Cause of a lower-tropospheric high-ozone layer in spring over Hanoi

S. -Y. Ogino[1], K. Miyazaki[2], M. Fujiwara[3], M. I. Nodzu[4], M. Shiotani[5], F. Hasebe[3], J. Matsumoto[1,4], J. Witte[6], A. M. Thompson[7], H. A. Nguyen-Thi[8], and T. V. Nguyen[8]

[1]Japan Agency for Marine-Earth Science and Technology, Yokosuka, Japan.

[2]Jet Propulsion Laboratory/California Institute for Technology, Pasadena, CA, USA

[3]Faculty of Environmental Earth Science, Hokkaido University, Sapporo, Japan.

[4]Department of Geography, Tokyo Metropolitan University, Hachioji, Japan.

[5]Research Institute for Sustainable Humanosphere, Kyoto University, Kyoto, Japan.

[6]National Center for Atmospheric Research, Earth Observing Laboratory, Colorado, USA.

[7]NASA Goddard Space Flight Center, Maryland, USA.

[8]Aero Meteorological Observatory, Viet Nam Meteorological and Hydrological Administration, Hanoi, Vietnam

Corresponding author: Shin-Ya Ogino (ogino-sy@jamstec.go.jp)

Key Points:

- Ozonesonde observations in Hanoi, Vietnam, for about fourteen years since 2004 display an ozone enhancement at ~3 km altitude in March–April
- Enhanced ozone air at ~3 km originates from burning areas west of Hanoi whereas low-ozone near-surface air is marine from the east
- Model experiments show biomass fires in the Indochina Peninsula are the cause of Hanoi's enhanced ozone

Abstract

The ozonesonde observations in Hanoi, Vietnam, over fourteen years since 2004 have confirmed the enhancement in lower tropospheric ozone concentration at about 3 km altitude in the spring season. We investigated the evolution of the ozone enhancement from analysis of meteorological data, backward trajectories, and model sensitivity experiments. In spring, air masses over Hanoi exhibit strong height dependence. At 3km, the high-ozone air masses originate from the land area to the west of Hanoi, while low-ozone air masses below about 1.5 km are from the oceanic area to the east. Above 4 km, the air masses are mostly traced back to the farther west area. The chemical transport model simulations revealed that precursor emissions from biomass burning in the inland Indochina Peninsula have the largest contribution to the lower tropospheric ozone enhancement, which is transported upward and eastward and overhangs the clean air intrusion from the ocean to the east of Hanoi. At this height level, the polluted air has the horizontal extent of about 20 degrees in longitude and latitude. The polluted air observed in Hanoi is transported further east and widely spread over the northern Pacific Ocean.

Plain Language Summary

Ozone in the lower atmosphere acts as an air pollutant and is one of the strong greenhouse gases. Understanding chemical and transport processes that control ozone variations provide important implications for the origin of air pollution and for climate change. In the past 20 years, the global tropospheric ozone amount has increased in the tropics and subtropics, with particularly large increases in Southeast Asia. We analyze a seasonal enhancement in ozone over Hanoi, Vietnam, using the 14-year record of upper air ozone measurements that began in 2004. The measurements reveal high levels of ozone particularly during the spring that peak at around 3 km. Numerical model simulations show that agricultural burning in the inland Indochina Peninsula is the major contributor to these high ozone amounts that are transported upward and eastward and overhang the clean air from the ocean to the east of Hanoi. Overtime, the high-ozone air observed in Hanoi is transported further east and widely spread over the northern Pacific Ocean. The identified source of the ozone enhancements and its three-dimensional distribution provide new insights into the impact of agricultural burning over Southeast Asia on large-scale ozone distributions and would benefit global air quality and climate studies.

1 Introduction

Tropospheric ozone is closely related with air quality by producing hydroxyl radicals which control oxidizing capacity of the atmosphere, and is itself an air pollutant and one of the strong greenhouse gases (Brasseur et al., 2003; IPCC, 2013). It is important to describe and understand the mechanism determining the three-dimensional (3D) distribution of ozone and its temporal variation in order to trace the origin of air pollution and to understand climate variability and change.

Because of the strong ozone production efficiency, changes in precursor emissions associated with economic and natural activity can lead to substantial changes in ozone in the tropics and subtropics (Cooper et al., 2020; Gaudel et al., 2020; Y. Zhang et al., 2021). While chemistry-climate models predict substantial changes in tropospheric ozone over these regions in the future climate scenarios (e. g., Morgenstern et al., 2017; Revell et al., 2018; Young et al., 2013), the multi model discrepancies remain large in predicted ozone and its radiative forcing (Kuai et al., 2020). Ozone in these regions is also important for human health associated with the

high population density and rapid economic development. However, the current in-situ observing network in these regions, for instance from Tropospheric Ozone Assessment Report (TOAR), is clearly insufficient for detailed evaluation of ozone changes for various applications including air pollutant human health impacts (Fleming et al., 2018). Studies using numerical models and limited observations have also illustrated the overall picture of non-local and local atmospheric pollution changes including ozone over South and Southeast Asia, such as wintertime northeasterly transports at low levels and summertime uplifting associated with Asian summer monsoon together with strong impacts of biomass burning (Lawrence & Lelieveld, 2010). Nevertheless, complete 3D structure of ozone in these regions and its driving factors remain unclear mainly due to a lack of detailed observational information. While long-term polar orbit and recent geostationary satellite measurements, such as Geostationary Environment Monitoring Spectrometer (GEMS) (Kim et al., 2020), can provide improved understanding of tropospheric ozone changes, vertical profile information from regular ozonesonde records are essential to study detailed chemical and physical processes.

Since September 2004, we have conducted regular ozonesonde observations once or twice a month in Hanoi (21.02°N, 105.80°E), Vietnam, on the Indochina Peninsula (Ogino et al., 2013), as part of the activities of Soundings of Ozone and Water in the Equatorial Region (SOWER; Hasebe et al., 2013) and Southern Hemisphere ADditional OZonesondes (SHADOZ; Thompson et al., 2012). Hanoi lies at the southeastern edge of the Asian summer monsoon circulation, which is a region of exchange of mass and chemical species between the tropical troposphere and the extratropical stratosphere in the Eastern Hemisphere. Southeast Asia is one of the important regions, where tropospheric ozone shows a long-term increasing trend, suggesting a significant contribution to global ozone change (Gaudel et al., 2018; Y. Zhang et al., 2016). In this regard, chemical and meteorological observations in Hanoi can provide valuable information about regional pollution and transport patterns.

Figure 1a shows the seasonal variation in the ozone mixing ratio (OMR) observed in Hanoi averaged over about fourteen years from September 2004 to June 2018. There are two height ranges with a large amplitude of seasonal variation. One is in the upper troposphere and lower stratosphere (UTLS) region (10–20 km), where ozone increases in spring (April to June) and summer (August), and decreases in winter, owing to the seasonal change of transport in the UTLS region. There is a northward transport of low-ozone air in winter due to the Rossby wave response to convective heating over the Maritime Continent and the western Pacific. This is followed by a southward transport of high-ozone air in summer due to the upper-tropospheric anticyclonic monsoon circulation associated with the South Asian High, as shown by Ogino et al. (2013). The other height range for large seasonal variability appears in the lower troposphere, with a peak OMR at around 3 km in the pre-monsoon season (March–April). This study aims to identify the origin of this peak OMR and propose a mechanism for the seasonal ozone enhancement.

Figure 2 shows the seasonal variation in the OMR up to 8 km height in the first half of the year, and the atmospheric stability, measured by the Brunt-Väisälä number. It shows two stable layers at ~1.5 and ~5 km in March, as reported by Nodzu et al. (2006). There is an ozone maximum between those layers that implies a distinct and separate feature.

Over the Indochina Peninsula, March is a transition period from the dry season to the rainy season. Intermittent rainfall begins in April (Kiguchi & Matsumoto, 2005; Matsumoto,

1997), and the summer monsoon season starts typically in May (He et al., 1987; Hsu et al., 1999; Nguyen-Le et al., 2015; Yanai et al., 1992), the earliest onset in the Asian monsoon region.

A similar but smaller ozone increase at the similar height and in the same season was observed in Hong Kong (22.31°N, 114.17°E) (L. Y. Chan et al., 1998; Ogino et al., 2013). Several authors showed that such ozone increases could be attributed to the transport of air polluted by biomass burning over Southeast Asia. Their analysis was based on backward trajectories that tend to pass over the active region of biomass burning, such as the Indian subcontinent and the northern Indochina Peninsula (C. Y. Chan, Chan, Chang, et al., 2003; C. Y. Chan, Chan, Harris, et al., 2003; C. Y. Chan & Chan, 2000; Liao et al., 2021). Liu et al. (2002) further confirmed that Southeast Asian biomass fires are responsible for the ozone enhancement observed in Hong Kong based on model simulations in which biomass burning emissions were eliminated. Recently, Liao et al. (2021) showed that the spring time ozone concentration above Hong Kong has an increasing trend possibly due to the biomass burning increase over the upwind region.

Burning activities are maximized in March over the northern part of the Indochina Peninsula (Huang et al., 2016), leading to enhanced surface ozone (Pochanart et al., 2001) and tropospheric column ozone (Sonkaew & Macatangay, 2015) in Thailand, an inland region of the Indochina Peninsula. These studies suggest that air polluted by biomass burning is a plausible cause of the ozone increase at about 3 km above Hanoi in March.

Most of the previous studies on the source of the ozone enhancement relied on backward trajectory analyses over Southeast Asia. However, traditional trajectory analysis does not provide any information on which emissions within Southeast Asia contributes most to the ozone enhancement quantitatively. It is also unclear why the ozone increase in March appears at about 3 km height above the surface. C. Y. Chan, Chan, Harris, et al. (2003) showed that the increase was accompanied by a stable layer at the bottom of the layer with the ozone increase, and mentioned that the inversion isolated the ozone rich layer from the influence of the local boundary layer. Nonetheless, the formation process and spatial distribution of the stable layer have not yet been fully described, and therefore, its relation to the high ozone layer is not clearly understood. The 3D structure of the ozone enhancement should be described by relating it to meteorological phenomena.

In this paper, we carry out a comprehensive study on the ozone enhancement with thermodynamic properties and the detailed analysis of chemical model sensitivity experiments. We first describe the variabilities of the ozone enhancement in March together with background meteorological properties, in which we identify three regimes in terms of ozone variability separated by the stable layers at about 1.5 km and about 4 km.

Next, we investigate the source region of ozone precursors that contributes the ozone enhancement above Hanoi by conducting sensitivity experiments using a chemical transport model with the observationally constrained top-down emissions. We further reveal the 3D structure of the ozone enhancement and investigate the mechanisms controlling the ozone enhancement that appears at about 3 km above Hanoi.

2 Data and methods

We used ozonesonde data collected at the Aero-Meteorological Observatory (21.02°N, 105.80°E), Hanoi, once or twice in each month from September 2004 to June 2018. The

observations are described in detail in Ogino et al. (2013). The data were re-processed in 2017 and 2018 (Witte et al., 2017, 2018) to obtain the homogenized data (SHADOZ Version 6 data sets). Total ozone from the soundings is in good agreement with satellite overpasses (e.g., from OMI and OMPS; Thompson et al., 2017; Witte et al., 2018) as well as from the Brewer spectrometer co-located at the Aero-Meteorological Observatory launch site. We used operational radiosonde data taken at the Observatory in Hanoi and the Japanese 55-year Reanalysis (JRA-55) objective analysis data (Kobayashi et al., 2015) to investigate meteorological fields.

The JRA-55 data were also used in back-trajectory calculations. Isentropic (without considering diabatic vertical motion) back-trajectories were calculated every 30 min using linearly interpolated JRA-55 meteorological reanalysis data (Kobayashi et al., 2015) and the second-order Runge-Kutta method for time integration, as in Hasebe et al. (2007) and Ogino et al. (2013). In each trajectory calculation, an initial point was set at every 200 m height from 100 m to the upper troposphere above Hanoi at the ozonesonde launch time in Hanoi.

To examine the relative importance of different emission source regions on the ozone enhancement above Hanoi, we performed sensitivity experiments using the global chemical-transport model, CHASER (Sudo et al., 2002) with T42 horizontal resolution (approximately 2.8° longitude × 2.8° latitude) and 32 vertical layers from the surface up to 10 hPa in sigma coordinate. The two-hourly model outputs interpolated onto the constant pressure levels at 1000, 990, 970, 930, 870, 790, 700, 610, 530, 460, 400, 350, 300, 260, 230, 200, 176, 153, 133, 116, 100, 88, 76, 66, 58, 50, 43, 36, 30, 22, 14, and 10 hPa were used in this study. Note that the updated model, MIROC-Chem (Miyazaki et al., 2017; Watanabe et al., 2011), includes more detailed chemical processes for both troposphere and stratosphere. Nevertheless, CHASER already includes the most important chemical processes in the NOx-CO-Ozone reactions and can be used to evaluate the impact of NOx emissions on ozone productions. In addition, the simulated ozone performance as well as ozone response to NOx emissions are comparable between CHASER and MIROC-Chem (Miyazaki et al., 2020). Thus, the results should not be sensitive to the choice of model.

The surface emission of major ozone precursors, such as carbon monoxide (CO), nitrogen oxide (NOx), and nonmethane hydrocarbons, were included in the model based on the published emission inventories (the Emission Database for Global Atmospheric Research (EDGAR) version 4.2 (EC-JRC/PBL, 2011), the monthly Global Fire Emissions Database (GFED) version 3.1 (van der Werf et al., 2010), and monthly mean Global Emissions Inventory Activity (GEIA) (Graedel et al., 1993)). We employed daily NOx and CO emissions that were optimized using the assimilation of satellite NO_2 and CO measurements, where the a priori emissions were constructed based upon bottom-up emission inventories (Miyazaki et al., 2015; 2017). These emissions, including both anthropogenic and biomass burning components, used were obtained from the Tropospheric Chemistry Reanalysis version 1 (TCR-1, Miyazaki et al., 2015) and enabled us to evaluate the emission impacts for individual sources.

In the sensitivity experiments we eliminated the emissions of ozone precursors from the following three source regions: the Indian subcontinent, the northern Indochina Peninsula, and southern China (Fig.3). We conducted spin-up calculations with the optimized emissions for all regions (i.e., standard emissions) from January 1st to the end of February in each year for 10 years from 2005 to 2014. Then, we performed four types of experiments from March 1st to 21st: the control experiment with the standard emissions (Fig. 3), and the three sensitivity experiments

with elimination of emission from the above-mentioned three regions, namely the Indian subcontinent, the northern Indochina, the southern China experiments. Because of the non-linear chemistry, the cumulative response from the sensitivity calculations can be different from the total ozone response in the control simulation to some extent as shown by the HTAP modeling works (Turnock et al., 2018; Wild et al., 2012). Nevertheless, they provided important information on relative contributions of emission sources from different regions. The results of the sensitivity experiments will be compared with the control experiment to investigate the relative contributions of individual emission sources to the ozone enhancement over Hanoi. Note that although the period of the model experiment (10 years) is shorter than that of the observation (about 14 years), we consider that the 10-year model data are sufficient for our purpose to describe the climatological feature of the ozone distribution.

3 Characteristics of ozone profiles in March

Figure 4a shows all of the vertical profiles of the OMR observed in Hanoi in March for the whole time period from 2005 to 2018. Figure 4b shows the vertical profiles of the Brunt-Väisälä number for the same ozonesonde observations. The profiles show that the ozone variability is large in three height ranges—0–1.5 km, 1.5–5 km, and 5–8 km—which are separated by two stable layers at ~1.5 and ~5 km first shown by Nodzu et al. (2006). For example, at 1.5–5 km, where the mean OMR in March peaked, the OMR is 50–120 ppbv. At 0–1.5 km the OMR was 0–100 ppbv, and at 5–8 km it is 30–80 ppbv. On the other hand, the variability in OMR is relatively small near the two stable layers at ~1.5 and ~5 km, at 50–80 ppbv. The large variability at the three height ranges is confirmed by calculating the standard deviation at each height as shown in Fig. 4c. Figure 4c also shows the frequency distribution of OMR at each height, in which we find different characteristics between the three height ranges. In 1.5–4 km, although the mode is about 60 ppbv, the distribution skews positively and the less-frequent large OMR values (> 80 ppbv) contribute to the ozone enhancement with the large mean value (75–80 ppbv) at this height range. In the layer above 5 km, the distribution shows slight negative skewness, and the mean values are smaller than those in 1.5–4 km, although the modes are similar to or slightly larger than those in 1.5–4.0 km. In the layer below 1.5 km, the frequency distribution skews positively, and both mode and mean decrease as height decrease.

Figure 5 shows three typical profiles of the ozone increases at 0–1.5 km (a), 1.5–5 km (b), and 5–8 km (c). On 26 April 2011 (Figure 5a), the OMR increased below the lower stable layer. On 12 March 2007 (Figure 5b), the height profile is similar to that seen in the fourteen-year-averaged height profile of March (Fig. 1b). This case also shows an ozone minimum at 0–1.5 km just below the lower stable layer. Note that there is also a sharp contrast in relative humidity between the levels below and above the lower stable layer: a humid (almost saturated) air mass below, and a relatively dry (about 40% RH) air mass above it. On 27 March 2009 (Figure 5c), the OMR increased above the upper stable layer at about 5 km.

The ozone increases in each of the three height ranges described above seem to be controlled by different mechanisms. Below, we investigate the mechanism of ozone variation in each layer. First, we investigate whether the ozone density above Hanoi depended on the origin of the air mass by using backward trajectory analysis. Next, we interpret the obtained typical trajectories in terms of transport processes and meteorological conditions.

4 Analysis of a typical case

First, we examine backward trajectories and atmospheric fields for a typical ozone increase at 1.5–5 km and for a typical ozone decrease at 0–1.5 km observed on 12 March 2007 shown in Fig. 5b. Figure 6 shows 5-day backward trajectories initialized at 0600 UT (launch time of the ozonesonde) on 12 March 2007 at every 200 m height above Hanoi. The backward trajectories show that the origins of the air masses differed between the height ranges above and below the lower stable layer at about 1.5 km. The air mass in the high-ozone layer at 1.5–4 km can be traced back to the Indochina Peninsula and nearby to the west of Hanoi. The air masses in the low-ozone layer below 1.5 km, on the other hand, originated from the South China Sea and the western Pacific area to the east of Hanoi. This difference is consistent with the observations of humid air below 1.5 km and dry air at 1.5–4 km mentioned in section 3. The change in ozone levels suggests that ozone concentration of the air mass from the Indochina Peninsula was enhanced by biomass burning, while that from the ocean areas was less polluted. The air masses above the upper stable layer (4–6 km) can be traced back to the farther west area than those at 1.5–4 km, suggesting that the mechanism that determines the ozone variation in this height range is different from those below about 4 km, and that the long-range transport, and various sources and source regions, such as air pollutions far from Hanoi and stratospheric ozone inputs, can contribute the ozone variations in this height range. In the rest of the paper, we mainly investigate and discuss the ozone variations in the surface-1.5 km and 1.5-4 km height ranges.

The pressure and temperature anomaly fields above Hanoi from 7 to 17 March 2007 (Figs. 7a, b) reveal a high-pressure, cold-temperature anomaly in the first half of the period. The Brunt-Väisälä number distribution shows clear stable layers at ~1.5 and ~4 km (Fig. 7c).

Figure 8a shows the horizontal distribution of the geopotential height and temperature of JRA-55 at 925 hPa on 10 March 2007, 2 days before the ozonesonde observation. The tongue-shaped high-pressure (Fig. 8a, yellow to red), and its associated low-temperature represents an intrusion from eastern China toward Hanoi due to the anti-cyclonic circulation. This structure is characteristic of a cold surge typically seen in winter and spring over Southeast Asia (Compo et al., 1999). The stable layer just above the cold air intrusion was strengthened locally near Hanoi as seen in Fig. 8b and c. Thus, the near-surface easterly flow bringing the low-ozone air mass from the ocean area shown by the backward trajectories in Fig. 6 was associated with this cold surge event, which simultaneously transports the cold air to produce the stable layer at about 850 hPa (about 1.5 km). Figure 8c also shows the development of unstable layer from the surface to about 600 hPa (4–5 km) above the land regions of the Indian Subcontinent and the Indochina Peninsula. This is likely caused by the development of a deep mixed boundary layer (0600UT corresponds to about noon time near the longitude region concerned) generated by the increased heating over the land surface through the seasonal transition from winter to summer (Nodzu et al., 2006; Ogino et al., 2010). This suggests that the polluted high-ozone air over the Indian Subcontinent and Indochina Peninsula can be lifted to 4–5 km level and be transported eastward to the ozone enhancement above Hanoi.

5 Model experiment

Here we use the chemical transport model simulations to further explore the relative contributions of individual emission source regions (c.f., Section 2). Figure 9 shows a time-height section of the 10-year mean of monthly mean OMR at the grid point near Hanoi in the control experiment using the standard optimized emissions constrained by satellite observations.

The control experiments well reproduce the seasonal variations in OMR. For instance, the simulated OMR reproduces the observed relative ozone maxima in March at about 700 hPa (about 3 km in height, Fig. 2), although the simulated peak value (65 ppbv) is smaller than the ozonesonde measured peak (85 ppbv) probably due to the coarser vertical resolution of the model and the model biases, such as the low stratospheric ozone input and the insufficient chemical production of ozone as suggested by Park et al. (2021). The model also well reproduces the observed relative timing and location of the seasonal and vertical distributions, such as the two maxima in May-June and September-October in the upper troposphere (400–200 hPa). About a one-month delay in the simulated seasonal march relative to the observed climatological variations in the upper troposphere implies systematic biases in the model chemical and physical processes, but it does not appear in the lower troposphere.

Temporal variability in ozone reproduced in the model shows similar features to the observation shown in Fig. 4. Figures 10a and 10c show that the ozone variability is large at three height ranges — 950–900 hPa (near-surface), 790–700 hPa (about 3 km, where the mean ozone maximum exists), and above 500 hPa — which are separated by the two stable layers at about 900 hPa and at 650–400 hPa. Frequency distribution (Fig. 10c) shows positive skewness at 790--700 hPa, and the outlying large ozone values contribute to the mean value at this pressure level, which is the same feature with the observational results shown in Fig. 4. Thus, the characteristic of ozone variability observed by the once- or twice-monthly ozonesondes was appropriately reproduced by the model experiment; conversely the ozonesonde observation has sampled ozone profiles without strong sampling biases.

At 700 hPa, the control experiment (Fig. 11a) reveals high OMR (> 62 ppbv) over each of the eastern parts of the two regions: the northeastern part of Indian subcontinent and northeastern part of the Indochina Peninsula. By eliminating the ozone precursor emission over the Indian subcontinent region, the ozone enhancement over northeast India disappears, whereas the one over the northeast Indochina Peninsula remains (Fig. 11b). The ozone enhancement over the northeastern part of the Indochina Peninsula, including the Hanoi location, was associated with emissions over the northern Indochina region (Fig. 11c). In the case of the southern China experiment, the Indochina signal remains (Fig. 11d). The contribution from emissions over each region can be more clearly seen by subtracting the result of each sensitivity experiment from that of the control experiment, as seen in Fig. 11e–g. We find that the Indochina emission produces the ozone enhancement above Hanoi and its impact at 700 hPa (about 3 km) spreads around Hanoi with horizontal extent of about 20 degrees in latitude and longitude (Fig. 11f).

In terms of vertical structure, the ozone enhancement above Hanoi originates from the northern Indochina emission (Fig. 12c, f). Figure 12f shows that the ozone enhancement over Indochina (93°E–106°E) is tilting and overhanging toward the east. This is the morphological reason why the ozone enhancement above Hanoi appears at about 3 km height above the surface. Thus, the overhanging ozone enhancement is formed by the polluted high-ozone air transport from the inland Indochina Peninsula over the clean oceanic air intrusion from the east near the surface. This picture is consistent with the backward trajectories for the typical case shown in the previous section (Fig. 6) and the zonal wind distribution shown in Fig. 13. Meanwhile, the distribution of carbon monoxide (CO) (Fig 14) almost coincides with that of ozone. Because of its direct emissions and relatively long lifetime in the atmosphere, enhanced CO in this region can be regarded as an indicator of air originated from biomass burning and less affected by stratospheric sources unlike ozone. The simultaneous enhancement of ozone and CO indicates

that the ozone enhancement occurs due to the biomass burning associated with slash-and-burn agriculture and agro-residue burning.

Figure 15a shows the vertical profiles of OMR above Hanoi obtained in the control and sensitivity experiments. The ozone enhancement appears at 700 hPa with the value of 66 ppbv in the control experiment. The OMR at the peak altitude (700 hPa) reduces to 63, 44, and 64 ppbv in the Indian Subcontinent, the northern Indochina, and the southern China experiments, respectively. The contributions of the ozone precursors emitted over the Indian Subcontinent, the northern Indochina, and the southern China regions on ozone at 700 hPa over Hanoi were estimated from the sensitivity experiments to be 3 ppbv (the Indian Subcontinent experiment), 21 ppbv (the northern Indochina experiment), and 2 ppbv (the southern China experiment) (Fig. 15b), accounting for 5% (the Indian Subcontinent experiment), 33% (the northern Indochina experiment), and 3% (the southern China experiment) changes (Fig. 15c), with additional 59% contributions from other regions. Although these values from the sensitivity experiment results involve ambiguity to some extent owing to the non-linear chemistry as mentioned in Section 2, they clearly highlight the dominant contribution from the northern Indochina region to the lower tropospheric ozone enhancement above Hanoi in spring.

Near the surface below the lower stable layer at about 1.5 km, the contribution from the southern China precursors is predominant (account for about 20% of ozone production), with almost negligible contributions from the Indian Subcontinent and the northern Indochina precursors (Fig. 15). The winter monsoon northeasterly could play a role in bringing the polluted air from the southern China region. This may seem inconsistent with the explanation that the intrusion of less polluted, oceanic air masses associated with the winter monsoon flow is responsible for the low mean ozone concentration the surface as mentioned in Section 4, but it can be reasonably interpreted as follows. Although the mean flow in March is almost easterly, the daily wind can fluctuate depending on the short time scale disturbances, such as cold surges, which resulted in the mixture of the dominant transport of the clean oceanic air from the east and of the intermittent intrusion of the polluted air from the south China region to the north and the northeast of Hanoi. Such an intermittent intrusion of high ozone event associated with the monsoon activities is a new insight for the near-surface ozone variation, details of which should be studied in a further investigation.

Finally, let us look at the global spread of ozone produced by the Northern Indochina emission. Figure 16 shows the ozone amount generated from the northern Indochina emission during March 1–20 in the middle troposphere (610 hPa). The chemical transport model suggests that ozone originating from northern Indochina can be transported widely eastward in the middle troposphere across the Pacific Ocean, and reach the North America and the North Atlantic Ocean, while the signals are also accumulated over the southern mid-latitudes in the middle troposphere. This feature has been reported by several studies based on the airplane experiments, such as Pacific Exploratory Mission-West (PEM-West) (Hoell et al., 1997) and Transport and Chemical Evolution Over the Pacific (TRACE-P) (Zhang et al., 2003). The present study has revealed the detailed and 3D structure near the source region and also over remote regions, which would provide important insights into the impact of biomass burning over Southeast Asia on global ozone distributions and radiation balance of the atmosphere. Further studies using the presented model simulations along with detailed validation using ozonesonde measurements would benefit global air quality and chemistry-climate studies, for instance, under the Hemispheric Transport of Air Pollution (HTAP) project.

6 Discussion

On the basis of the analyses of backward trajectories, meteorological fields, and the numerical experiments, we propose a mechanism, illustrated in Fig. 17, for the increase of ozone frequently observed at ~3 km above Hanoi in March. During this month, the atmosphere is relatively unstable, allowing shallow convection to develop below the upper stable layer at ~5 km over the inland Indochina Peninsula and the Indian Subcontinent. It is well known that the occurrence of biomass burning in these regions increases during February to April (Huang et al., 2016). The near-surface polluted air is well mixed by shallow convection up to the height of the upper stable layer. This well-mixed air is advected by the westerly flow; but the air below the lower stable layer is blocked by the near-surface easterly flow with the oceanic, less-polluted airmass, and only the air above the lower stable layer can reach the eastern region of the Indochina Peninsula. The main source of the enhanced ozone above Hanoi originates from the ozone precursors emitted over the northern part of the Indochina Peninsula. The polluted high-ozone air at the peak height covers the region with a horizontal scale of about 20 degrees in longitude and latitude over the northeastern part of the Indochina Peninsula around Hanoi. The airmasses are transported further eastward and upward and spread over the northern Pacific Ocean in the middle troposphere.

This mechanism occurs from March to April, because land heating is not strong enough in January and shallow convection does not reach 4–5 km as a result (Nodzu et al., 2006). Also it is before the rainy season that starts in May over the Indochina Peninsula (e.g., He et al., 1987; Hsu et al., 1999; Yanai et al., 1992). Thus, the ozone transport and distribution from March to April are characterized not only by the seasonality of biomass burning, but also by the monsoon transition from the dry season to the rainy season.

Our results show that the ozone increase at ~3 km in March above Hanoi resembles that seen over Hong Kong. A polluted air mass from the same origin may sometimes pass over both Hanoi and Hong Kong. Such polluted air masses are considered to originate from the north of the Indochina Peninsula, which is closer to Hanoi than to Hong Kong. This is consistent with the fact that the climatological signal of the ozone increase is clearer in Hanoi than in Hong Kong as seen in Fig. 1 of Ogino et al. (2013).

We showed that a stable layer (at ~5 km) exists at the top of the ozone increase, adding to the finding of the stable layer at the bottom of the ozone increase by L. Y. Chan et al. (2000) and C. Y. Chan et al. (2003). The ozone increase appears between two stable layers at ~1.5 and ~5 km. The ozone density above the upper stable layer seems to be separated from that below it and is controlled by a different mechanism. L. Y. Chan et al. (2000) and C. Y. Chan et al. (2003) stated that the lower stable layer isolates the layer with the ozone increase at ~3 km from the influence of the local boundary layer. We add that the horizontal advection of clean, oceanic air associated with the cold surge passage is essential for the isolation.

Recent studies suggested that stratospheric ozone intrusion plays an important role in tropospheric ozone variations including the spring ozone enhancement in spring above Hong Kong (Liao et al., 2021; Zhao, Hu, et al., 2021; Zhao, Huang, et al., 2021). Although we cannot discuss quantitatively the stratospheric contribution to the spring ozone enhancement above Hanoi, because the experiment in this study tested the sensitivity to the surface emissions of ozone precursors, a certain amount of stratospheric ozone can contribute to the spring ozone enhancement above Hanoi. However, if we look at the spatial distribution as seen in Figs. 12 and

13, the observed ozone enhancement in the lower troposphere above Hanoi is clearly connected with the surface emission over the Indochina Peninsula. In any case, the geographical difference between Hong Kong and Hanoi can lead to different stratospheric contributions. The 3D transport process should be clarified in more detail in future investigations to understand the relative importance of stratospheric intrusion.

7 Conclusions

Regular ozonesonde observations for about fourteen years above Hanoi revealed an ozone increase at ~3 km in March. The ozone densities in March showed large temporal variability at three height ranges that are separated by two stable layers at ~1.5 and ~5 km. Meteorological and backward trajectory analyses showed that a typical ozone enhancement at ~3 km originated from air polluted over the Indochina Peninsula and a typical decrease below 1.5 km was caused by the advection of the clean oceanic air associated with a cold surge event.

We conducted a sensitivity experiment using a chemical transport model, in which we eliminated the emissions of ozone precursors (CO and NO_2) in three regions (the Indian Subcontinent, the northern Indochina, and southern China). The ozone concentration above Hanoi was most effectively suppressed when emissions of ozone precursors over northern Indochina Peninsula are eliminated. This suggests that air pollution from northern Thailand (probably due to biomass burning) contributed most to the ozone increase in Hanoi. The model showed that the ozone increase originated from the northern Indochina Peninsula emission expanded in the lower troposphere over an area of about 20 degrees in longitude and latitude. The model also reproduced the ozone decrease near the surface due to the clean air intrusion associated with the winter monsoon easterly wind. The polluted air was further transported eastward into the middle and upper troposphere across the Pacific Ocean, and some of it reached the west coast of the USA.

We propose that the ozone increase at 3 km over Hanoi in March was caused by the eastward advection of polluted, high-ozone air that was well mixed up to the stable layer at ~5 km over the land mass of the Indochina Peninsula to the west of Hanoi, and by the westward advection of less-polluted, low-ozone air from the oceanic area to the east of Hanoi associated with a cold surge event below the stable layer at ~1.5 km. Such a mechanism occurs only between March and April, after the development of active shallow convection and before the start of summer monsoon rainfall. We conclude that the ozone enhancement over Southeast Asia is caused not only by the biomass burning enhancement, but also by atmospheric circulation system formed in pre-monsoon season. The circulation system determines the detailed 3D structure of ozone distribution.

Acknowledgments

This work was supported by JSPS KAKENHI Grant Numbers JP15204043, JP18204041, JP21244072, JP26220101, and JP16K00535. The SHADOZ sondes at Hanoi are supported by NASA's Upper Atmosphere Research Program through funding to Goddard Space Flight Center (Maryland USA) and the Ozone group at NOAA's Global Monitoring Lab (Colorado USA); special thanks to Patrick Cullis (CIRES at NOAA). Part of this work was conducted at the Jet Propulsion Laboratory, California Institute of Technology, under contract with the National Aeronautics and Space Administration (NASA).

Data Availability Statement

The ozonesonde data used in this study are available in the SHADOZ archive https://tropo.gsfc.nasa.gov/shadoz/ (SHADOZ, 2018). JRA-55 data can be obtained from the Japan Meteorological Agency http://jra.kishou.go.jp/JRA-55/index_en.html (Japan Meteorological Agency, 2018). The radiosonde data at the Hanoi station are available in the archive site of University of Wyoming http://weather.uwyo.edu/upperair/sounding.html (Wyoming University, 2018). The data of the numerical experiment presented in Sec. 5 are available at https://doi.org/10.5281/zenodo.6459880 (Miyazaki, 2022).

References

Brasseur, G. P., Prinn, R. G., & Pszenny, A. A. P. (Eds.). (2003). *Atmospheric Chemistry in a Changing World*. Berlin: Springer-Verlag. Retrieved from http://www.springer.com/earth+sciences+and+geography/meteorology+&+climatology/book/978-3-540-43050-6

Chan, C. Y., & Chan, L. Y. (2000). Effect of meteorology and air pollutant transport on ozone episodes at a subtropical coastal Asian city, Hong Kong. *Journal of Geophysical Research: Atmospheres*, *105*(D16), 20707–20724. https://doi.org/10.1029/2000JD900140

Chan, C. Y., Chan, L. Y., Chang, W. L., Zheng, Y. G., Cui, H., Zheng, X. D., et al. (2003). Characteristics of a tropospheric ozone profile and implications for the origin of ozone over subtropical China in the spring of 2001. *Journal of Geophysical Research: Atmospheres*, *108*(20), 1–14. https://doi.org/10.1029/2003jd003427

Chan, C. Y., Chan, L. Y., Harris, J. M., Oltmans, S. J., Blake, D. R., Qin, Y., et al. (2003). Characteristics of biomass burning emission sources, transport, and chemical speciation in enhanced springtime tropospheric ozone profile over Hong Kong. *Journal of Geophysical Research: Atmospheres*, *108*(1). https://doi.org/10.1029/2001jd001555

Chan, L. Y., Liu, H. Y., Lam, K. S., Wang, T., Oltmans, S. J., & Harris, J. M. (1998). Analysis of the seasonal behavior of tropospheric ozone at Hong Kong. *Atmospheric Environment*, *32*(2), 159–168. https://doi.org/10.1016/S1352-2310(97)00320-8

Chan, L. Y., Chan, C. Y., Liu, H. Y., Christopher, S., Oltmans, S. J., & Harris, J. M. (2000). A case study on the biomass burning in southeast Asia and enhancement of tropospheric ozone over Hong Kong. *Geophysical Research Letters*, *27*(10), 1479. https://doi.org/10.1029/1999GL010855

Compo, G. P., Kiladis, G. N., & Webster, P. J. (1999). The horizontal and vertical structure of east Asian winter monsoon pressure surges. *Quarterly Journal of the Royal Meteorological Society*, *125*, 29–54. https://doi.org/10.1002/qj.49712555304

Cooper, O. R., Schultz, M. G., Schröder, S., Chang, K. L., Gaudel, A., Benítez, G. C., et al. (2020). Multi-decadal surface ozone trends at globally distributed remote locations. *Elementa*, *8*(23). https://doi.org/10.1525/elementa.420

EC-JRC/PBL – European Commission, Joint Research Centre/Netherlands Environmental Assessment Agency PBL (2011). Emission Database for Global Atmospheric Research (EDGAR), Release Version 4.2. Retrieved from http://edgar.jrc.ec.europa.eu/

Fleming, Z. L., Doherty, R. M., von Schneidemesser, E., Malley, C. S., Cooper, O. R., Pinto, J. P., et al. (2018). Tropospheric Ozone Assessment Report: Present-day ozone distribution and trends relevant to human health. *Elementa: Science of the Anthropocene*, *6*. https://doi.org/10.1525/elementa.273

Gaudel, A., Cooper, O. R., Ancellet, G., Barret, B., Boynard, A., Burrows, J. P., et al. (2018). Tropospheric Ozone Assessment Report: Present-day distribution and trends of tropospheric ozone relevant to climate and global atmospheric chemistry model evaluation. *Elementa*, *6*. https://doi.org/10.1525/elementa.291

Gaudel, A., Cooper, O. R., Chang, K. L., Bourgeois, I., Ziemke, J. R., Strode, S. A., et al. (2020). Aircraft observations since the 1990s reveal increases of tropospheric ozone at multiple locations across the Northern Hemisphere. *Science Advances*, *6*(34), eaba8727. https://doi.org/10.1126/sciadv.aba8272

Graedel, T. E., Bates, T. S., Bouwman, A. F., Cunnold, D., Dignon, J., Fung, I., et al. (1993). A compilation of inventories of emissions to the atmosphere. *Global Biogeochemical Cycles*, *7*(1), 1–26. https://doi.org/https://doi.org/10.1029/92GB02793

Hasebe, F., Fujiwara, M., Nishi, N., Shiotani, M., Vömel, H., Oltmans, S., et al. (2007). In situ observations of dehydrated air parcels advected horizontally in the Tropical Tropopause Layer of the western Pacific. *Atmospheric Chemistry and Physics*, *7*(3), 803–813. https://doi.org/10.5194/acp-7-803-2007

Hasebe, F., Inai, Y., Shiotani, M., Fujiwara, M., Vömel, H., Nishi, N., et al. (2013). Cold trap dehydration in the Tropical Tropopause Layer characterised by SOWER chilled-mirror hygrometer network data in the Tropical Pacific. *Atmospheric Chemistry and Physics*, *13*(8), 4393–4411. https://doi.org/10.5194/acp-13-4393-2013

He, H., McGinnis, J. W., Song, Z., & Yanai, M. (1987). Onset of the Asian summer monsoon in 1979 and the effect of the Tibetan Plateau. *Monthly Weather Review*, *115*(9), 1966–1995. https://doi.org/10.1175/1520-0493(1987)115<1966:OOTASM>2.0.CO;2

Hoell, J. M., Davis, D. D., Liu, S. C., Newell, R. E., Akimoto, H., McNeal, R. J., & Bendura, R. J. (1997). The Pacific Exploratory Mission-West Phase B: February-March, 1994. *Journal of Geophysical Research: Atmospheres*, *102*(D23), 28223–28239. https://doi.org/10.1029/97JD02581

Hsu, H.-H., Terng, C.-T., & Chen, C.-T. (1999). Evolution of large-scale circulation and heating during the first transition of Asian summer monsoon. *Journal of Climate*, *12*(3), 793–810. https://doi.org/10.1175/1520-0442(1999)012<0793:EOLSCA>2.0.CO;2

Huang, W.-R., Wang, S.-H., Yen, M.-C., Lin, N.-H., & Promchote, P. (2016). Interannual variation of springtime biomass burning in Indochina: Regional differences, associated atmospheric dynamical changes, and downwind impacts. *Journal of Geophysical Research: Atmospheres*, *121*(17), 10016–10028. https://doi.org/10.1002/2016JD025286

IPCC. (2013). *Climate Change 2013: The Physical Science Basis, Contribution of Working Group I to the Fifth Assessment Report of the Intergovernmental Panel on Climate Change*. (T. F. Stocker, D. Qin, G. K. Plattner, M. M. B. Tignor, S. K. Allen, J. Boschung, et al., Eds.). Cambridge, United Kingdom and New Yourk, NY, USA: Cambridge University Press.

Japan Meteorological Agency (2018). The Japanese 55-year Reanalysis [Dataset]. https://jra.kishou.go.jp/JRA-55/. Retrieved in 2018.

Kiguchi, M., & Matsumoto, J. (2005). The rainfall phenomena during the pre-monsoon period over the Indochina Peninsula in the GAME-IOP year, 1998. *Journal of the Meteorological Society of Japan. Ser. II*, *83*(1), 89–106. https://doi.org/10.2151/jmsj.83.89

Kim, J., Jeong, U., Ahn, M.-H., Kim, J. H., Park, R. J., Lee, H., et al. (2020). New era of air quality monitoring from space: Geostationary Environment Monitoring Spectrometer (GEMS). *Bulletin of the American Meteorological Society*, *101*(1), E1–E22. https://doi.org/10.1175/BAMS-D-18-0013.1

Kobayashi, S., Ota, Y., Harada, Y., Ebita, A., Moriya, M., Onoda, H., et al. (2015). The JRA-55 reanalysis: General specifications and basic characteristics. *Journal of the Meteorological Society of Japan. Ser. II*, *93*(1), 5–48. https://doi.org/10.2151/jmsj.2015-001

Kuai, L., Bowman, K. W., Miyazaki, K., Deushi, M., Revell, L., Rozanov, E., et al. (2020). Attribution of Chemistry-Climate Model Initiative (CCMI) ozone radiative flux bias from satellites. *Atmospheric Chemistry and Physics*, *20*(1), 281–301. https://doi.org/10.5194/acp-20-281-2020

Lawrence, M. G., & Lelieveld, J. (2010). Atmospheric pollutant outflow from southern Asia: A review. *Atmospheric Chemistry and Physics*, *10*(22), 11017–11096. https://doi.org/10.5194/acp-10-11017-2010

Liao, Z., Ling, Z., Gao, M., Sun, J., Zhao, W., Ma, P., et al. (2021). Tropospheric ozone variability over Hong Kong based on recent 20-year (2000–2019) ozonesonde observation. *Journal of Geophysical Research: Atmospheres*, *126*(3). https://doi.org/10.1029/2020jd033054

Liu, H., Jacob, D. J., Chan, L. Y., Oltmans, S. J., Bey, I., Yantosca, R. M., et al. (2002). Sources of tropospheric ozone along the Asian Pacific Rim: An analysis of ozonesonde observations. *Journal of Geophysical Research: Atmospheres*, *107*(D21), ACH 3-1-ACH 3-19. https://doi.org/10.1029/2001JD002005

Matsumoto, J. (1997). Seasonal transition of summer rainy season over indochina and adjacent monsoon region. *Advances in Atmospheric Sciences*, *14*(2), 231–245. https://doi.org/10.1007/s00376-997-0022-0

Miyazaki, K., Eskes, H. J., & Sudo, K. (2015). A tropospheric chemistry reanalysis for the years 2005–2012 based on an assimilation of OMI, MLS, TES, and MOPITT satellite data. *Atmospheric Chemistry and Physics*, *15*(14), 8315–8348. https://doi.org/10.5194/acp-15-8315-2015

Miyazaki, K., Eskes, H., Sudo, K., Folkert Boersma, K., Bowman, K., & Kanaya, Y. (2017). Decadal changes in global surface NOx emissions from multi-constituent satellite data assimilation. *Atmospheric Chemistry and Physics*, *17*(2), 807–837. https://doi.org/10.5194/acp-17-807-2017

Miyazaki, K., Bowman, W. K., Yumimoto, K., Walker, T., & Sudo, K. (2020). Evaluation of a multi-model, multi-constituent assimilation framework for tropospheric chemical reanalysis. *Atmospheric Chemistry and Physics*, *20*(2), 931–967. https://doi.org/10.5194/acp-20-931-2020

583 Miyazaki, K (2022). Sensitivity experiment data using the CHASER chemical transport model
584 for investigation of lower-tropospheric spring ozone enhancement over Hanoi [Data set].
585 Zenodo. https://doi.org/10.5281/zenodo.6459880

586 Morgenstern, O., Hegglin, M., Rozanov, E., O'Connor, F., Luke Abraham, N., Akiyoshi, H., et
587 al. (2017). Review of the global models used within phase 1 of the Chemistry-Climate
588 Model Initiative (CCMI). *Geoscientific Model Development*, *10*(2), 639–671.
589 https://doi.org/10.5194/gmd-10-639-2017

590 Nguyen-Le, D., Matsumoto, J., & Ngo-Duc, T. (2015). Onset of the rainy seasons in the eastern
591 Indochina Peninsula. *Journal of Climate*, *28*(14), 5645–5666. https://doi.org/10.1175/JCLI-
592 D-14-00373.1

593 Nodzu, M. I., Ogino, S.-Y., Tachibana, Y., & Yamanaka, M. D. (2006). Climatological
594 description of seasonal variations in lower-tropospheric temperature inversion layers over
595 the Indochina Peninsula. *Journal of Climate*, *19*(13), 3307–3319.
596 https://doi.org/10.1175/JCLI3792.1

597 Ogino, S.-Y., Nodzu, M. I., Tachibana, Y., Matsumoto, J., Yamanaka, M. D., & Watanabe, A.
598 (2010). Temperature inversions over the Inland Indochina revealed by GAME-T enhanced
599 rawinsonde observations. *SOLA*, *6*, 5–8. https://doi.org/10.2151/sola.2010-002

600 Ogino, S.-Y., Fujiwara, M., Shiotani, M., Hasebe, F., Matsumoto, J., T. Hoang, T. H., & T.
601 Nguyen, T. T. (2013). Ozone variations over the northern subtropical region revealed by
602 ozonesonde observations in Hanoi. *Journal of Geophysical Research: Atmospheres*, *118*(8),
603 3245–3257. https://doi.org/10.1002/jgrd.50348

604 Park, R. J., Oak, Y. J., Emmons, L. K., Kim, C. H., Pfister, G. G., Carmichael, G. R., et al.
605 (2021). Multi-model intercomparisons of air quality simulations for the KORUS-AQ
606 campaign. *Elementa*, *9*(1). https://doi.org/10.1525/elementa.2021.00139

607 Pochanart, P., Kreasuwun, J., Sukasem, P., Geeratithadaniyom, W., Tabucanon, M. S.,
608 Hirokawa, J., et al. (2001). Tropical tropospheric ozone observed in Thailand. *Atmospheric*
609 *Environment*, *35*(15), 2657–2668. https://doi.org/10.1016/S1352-2310(00)00441-6

610 Revell, L. E., Stenke, A., Tummon, F., Feinberg, A., Rozanov, E., Peter, T., et al. (2018).
611 Tropospheric ozone in CCMI models and Gaussian process emulation to understand biases
612 in the SOCOLv3 chemistry-climate model. *Atmospheric Chemistry and Physics*, *18*(21),
613 16155–16172. https://doi.org/10.5194/acp-18-16155-2018

614 SHADOZ (2021). Ozonesonde data (Version 6) [Dataset]. https://tropo.gsfc.nasa.gov/shadoz/,
615 Retrieved in 2021.

616 Sonkaew, T., & Macatangay, R. (2015). Determining relationships and mechanisms between
617 tropospheric ozone column concentrations and tropical biomass burning in Thailand and its
618 surrounding regions. *Environmental Research Letters*, *10*(6). https://doi.org/10.1088/1748-
619 9326/10/6/065009

620 Sudo, K., Takahashi, M., Kurokawa, J., & Akimoto, H. (2002). CHASER : A global chemical
621 model of the troposphere 1 . Model description. *Journal of Geophysical Research*,
622 *107*(D17), 4339. https://doi.org/10.1029/2001JD001113

Thompson, A. M., Miller, S. K., Tilmes, S., Kollonige, D. W., Witte, J. C., Oltmans, S. J., et al. (2012). Southern Hemisphere Additional Ozonesondes (SHADOZ) ozone climatology (2005–2009): Tropospheric and tropical tropopause layer (TTL) profiles with comparisons to OMI-based ozone products. *Journal of Geophysical Research Atmospheres*, *117*(23), 1–27. https://doi.org/10.1029/2011JD016911

Thompson, A. M., Witte, J. C., Sterling, C., Jordan, A., Johnson, B. J., Oltmans, S. J., et al. (2017). First reprocessing of Southern Hemisphere ADditional OZonesondes (SHADOZ) ozone profiles (1998–2016): 2. Comparisons with satellites and ground-based instruments. *Journal of Geophysical Research: Atmospheres*, *122*(23). https://doi.org/10.1002/2017JD027406

Turnock, S. T., Wild, O., Dentener, F. J., Davila, Y., Emmons, L. K., Flemming, J., et al. (2018). The impact of future emission policies on tropospheric ozone using a parameterised approach. *Atmospheric Chemistry and Physics*, *18*(12), 8953–8978. https://doi.org/10.5194/acp-18-8953-2018

University of Wyoming (2018). Radiosonde data [Dataset]. http://weather.uwyo.edu/upperair/sounding.html. Retrieved in 2018.

Watanabe, S., Hajima, T., Sudo, K., Nagashima, T., Takemura, T., Okajima, H., et al. (2011). MIROC-ESM 2010: Model description and basic results of CMIP5-20c3m experiments. *Geoscientific Model Development*, *4*(4), 845–872. https://doi.org/10.5194/gmd-4-845-2011

van der Werf, G. R., Randerson, J. T., Giglio, L., Collatz, G. J., Mu, M., Kasibhatla, P. S., et al. (2010). Global fire emissions and the contribution of deforestation, savanna, forest, agricultural, and peat fires (1997-2009). *Atmospheric Chemistry and Physics*, *10*(23), 11707–11735. https://doi.org/10.5194/acp-10-11707-2010

Wild, O., Fiore, A. M., Shindell, D. T., Doherty, R. M., Collins, W. J., Dentener, F. J., et al. (2012). Modelling future changes in surface ozone: A parameterized approach. *Atmospheric Chemistry and Physics*, *12*(4), 2037–2054. https://doi.org/10.5194/acp-12-2037-2012

Witte, J. C., Thompson, A. M., Smit, H. G. J., Fujiwara, M., Posny, F., Coetzee, G. J. R., et al. (2017). First reprocessing of Southern Hemisphere ADditional OZonesondes (SHADOZ) profile records (1998–2015): 1. Methodology and evaluation. *Journal of Geophysical Research*, *122*(12), 6611–6636. https://doi.org/10.1002/2016JD026403

Witte, J. C., Thompson, A. M., Smit, H. G. J., Vömel, H., Posny, F., & Stübi, R. (2018). First reprocessing of Southern Hemisphere ADditional OZonesondes profile records: 3. Uncertainty in ozone profile and total column. *Journal of Geophysical Research: Atmospheres*, *123*(6), 3243–3268. https://doi.org/10.1002/2017JD027791

Yanai, M., Li, C., & Song, Z. (1992). Seasonal heating of the Tibetan Plateau and its effects on the evolution of the Asian summer monsoon. *Journal of the Meteorological Society of Japan. Ser. II*, *70*(1B), 319–351. https://doi.org/10.2151/jmsj1965.70.1B_319

Young, P. J., Archibald, A. T., Bowman, K. W., Lamarque, J.-F., Naik, V., Stevenson, D. S., et al. (2013). Pre-industrial to end 21st century projections of tropospheric ozone from the Atmospheric Chemistry and Climate Model Intercomparison Project (ACCMIP). *Atmospheric Chemistry and Physics*, *13*(4), 2063–2090. https://doi.org/10.5194/acp-13-2063-2013

Zhang, M., Uno, I., Carmichael, G. R., Akimoto, H., Wang, Z., Tang, Y., et al. (2003). Large-scale structure of trace gas and aerosol distributions over the western Pacific Ocean during the Transport and Chemical Evolution Over the Pacific (TRACE-P) experiment. *Journal of Geophysical Research D: Atmospheres*, *108*(21). https://doi.org/10.1029/2002jd002946

Zhang, Y., Cooper, O. R., Gaudel, A., Thompson, A. M., Nédélec, P., Ogino, S.-Y., & West, J. J. (2016). Tropospheric ozone change from 1980 to 2010 dominated by equatorward redistribution of emissions. *Nature Geoscience*, *9*(12), 875–879. https://doi.org/10.1038/ngeo2827

Zhang, Y., West, J. J., Emmons, L. K., Flemming, J., Jonson, J. E., Lund, M. T., et al. (2021). Contributions of world regions to the global tropospheric ozone burden change from 1980 to 2010. *Geophysical Research Letters*, *48*(1). https://doi.org/10.1029/2020GL089184

Zhao, K., Hu, C., Yuan, Z., Xu, D., Zhang, S., Luo, H., et al. (2021). A modeling study of the impact of stratospheric intrusion on ozone enhancement in the lower troposphere over the Hong Kong regions, China. *Atmospheric Research*, *247*(February 2020), 105158. https://doi.org/10.1016/j.atmosres.2020.105158

Zhao, K., Huang, J., Wu, Y., Yuan, Z., Wang, Y., Li, Y., et al. (2021). Impact of Stratospheric Intrusions on Ozone Enhancement in the Lower Troposphere and Implication to Air Quality in Hong Kong and Other South China Regions. *Journal of Geophysical Research: Atmospheres*, *126*(18), 1–19. https://doi.org/10.1029/2020JD033955

Figure captions

Figure 1. (a) Fourteen-year-averaged seasonal variation in ozone mixing ratio (OMR) obtained by calculating monthly-mean values at each height to 20 km from September 2004 to June 2018. Each monthly-mean value is plotted at each vertical dotted line. (b) Vertical profiles of annual-mean OMR (dashed line), standard deviation of fourteen-year-averaged seasonal variation in OMR (thin solid line), and standard deviation normalized by the annual-mean OMR at each height (thick solid line). These panels update Fig. 1 in Ogino et al. (2013) by adding seven years data.

Figure 2. Fourteen-year-averaged seasonal variation in ozone mixing ratio obtained by calculating monthly-mean values at each height to 8 km from January to June from 2004 to 2018. Black contours show fourteen-year-averaged seasonal variation of the Brunt-Väisälä number ($rad^2\ s^{-2} \times 10^4$). Each monthly-mean value is plotted at each vertical dotted line.

Figure 3. The rectangles show the regions where the ozone precursor emissions were eliminated in the sensitivity experiments: (Blue) the Indian Subcontinent, (Green) the northern Indochina Peninsula, and (Red) southern China. The gray shade shows the (a) carbon monoxide and (b) nitrogen oxide emissions from the surface in March averaged for 10 years from 2005 to 2014 adopted in the control run of the numerical experiment. A cross mark shows the location of Hanoi, Vietnam.

Figure 4. Vertical profiles of (a) ozone mixing ratio and (b) Brunt-Väisälä number observed by the ozonesondes in March for the whole time period (2005–2018). Blue line shows the mean of all data in each panel. (c) Frequency distribution (shade), the mean (white solid line) and one standard deviation on the either side of the mean (white dashed line) of ozone mixing ratio.

Figure 5. Vertical profiles of the ozone mixing ratio (red), the Brunt-Väisälä number (blue), and relative humidity (black) on (a) April 26, 2011, (b) March 12, 2007, and (c) March 27, 2009.

Figure 6. Backward trajectories initialized at 0600 UT on 12 March 2007 plotted on (a) longitude-height section and (b) longitude-latitude section. Color of each trajectory differs depending on its starting height as found in ○.

Figure 7. Time-height sections of (a) pressure anomaly, (b) temperature anomaly, and (c) Brunt-Väisälä number (N^2) drawn from operational radiosonde data collected in Hanoi from 7 to 17 March 2007. The anomalies are deviations from the 10-day mean at each height. Vertical solid line denotes the ozonesonde observation at 0600 UT on 12 March 2007.

Figure 8. Horizontal distributions of (a) geopotential height (colors) and temperature (contours) at 925 hPa, (b) vertical stability (vertical gradient of potential temperature $-\partial\theta/\partial p$) at 862.5 hPa, and (c) longitude-pressure section of vertical stability at 20°N at 0600 UT on 10 March 2007 drawn with JRA-55 data. The regions under the ground surface are masked with white color. Black cross marks in ○ and ○ denote the location of Hanoi. A white vertical line in ○ denotes the longitude of Hanoi.

Figure 9. Time-height cross section of the 10-year mean of monthly mean OMR at the grid near Hanoi reproduced in the control experiment of the sensitivity experiments using the chemical

transport model, CHASER. Each monthly-mean value is plotted at each vertical dotted line. The regions under the ground surface are masked with white color.

Figure 10. Vertical profiles of (a) ozone mixing ratio and (b) vertical gradient of potential temperature reproduced in the control experiment. All the 2-hourly profiles in March 1–21 for 10 years from 2005 to 2014 are plotted in grey lines, and the mean of each parameter is plotted in blue line in each panel. (c) Frequency distribution (shade), the mean (white solid line) and one standard deviation on the either side of the mean (white dashed line) of ozone mixing ratio.

Figure 11. The mean horizontal ozone distributions at 700 hPa for the period from March 1st to 20th obtained from the 10-year sensitivity model experiments. (Upper panels) Ozone mixing ratio for (a) the control, (b) the Indian subcontinent, (c) the northern Indochina, and (d) the southern China experiments. (Lower panels) The ozone production due to the ozone precursors emitted from (e) the Indian subcontinent, (f) the northern Indochina, and (g) the southern China regions. A cross mark in each panel shows the location of Hanoi. The regions under the ground surface are masked with white color.

Figure 12. Same as Fig. 11 but for zonal-vertical sections at 20.9°N. Contours show the vertical stability estimated by vertical gradient of potential temperature in unit of 10^2 K/hPa. A white vertical line in each panel shows the longitude of Hanoi.

Figure 13. Zonal-vertical section of the zonal wind at 20.9°N reproduced in the control experiment. Contours show the vertical stability estimated by the vertical gradient of potential temperature in unit of 10^2 K/hPa. A white vertical line shows the longitude of Hanoi. The regions under the ground surface are masked with white color.

Figure 14. As in Fig. 13, but for the CO mixing ratio in the control experiment.

Figure 15. Vertical profiles of (a) ozone mixing ratio obtained from the sensitivity experiment over the model gridpoint nearest to Hanoi. Each line represents a result from (black) the control, (blue) the Indian Subcontinent, (green) the Northern Indochina, and (red) the Southern China experiment. (b) Its difference between the control experiment and each of the sensitivity experiment, which means ozone mixing ratio contribution from each emission region, and (c) contribution percentage due to the ozone precursor emission in each sensitivity experiment (obtained by dividing the difference values show in (b) by the amount obtained from the control experiment shown by the black line in (a)) are also shown.

Figure 16. Global distribution of ozone mixing ratio at 610 hPa obtained from the difference between the control experiment and the northern Indochina experiment. A cross mark denotes the location of Hanoi.

Figure 17. Schematic diagram of the proposed mechanism for the ozone increase at 3 km above Hanoi in March.

Figure 1.

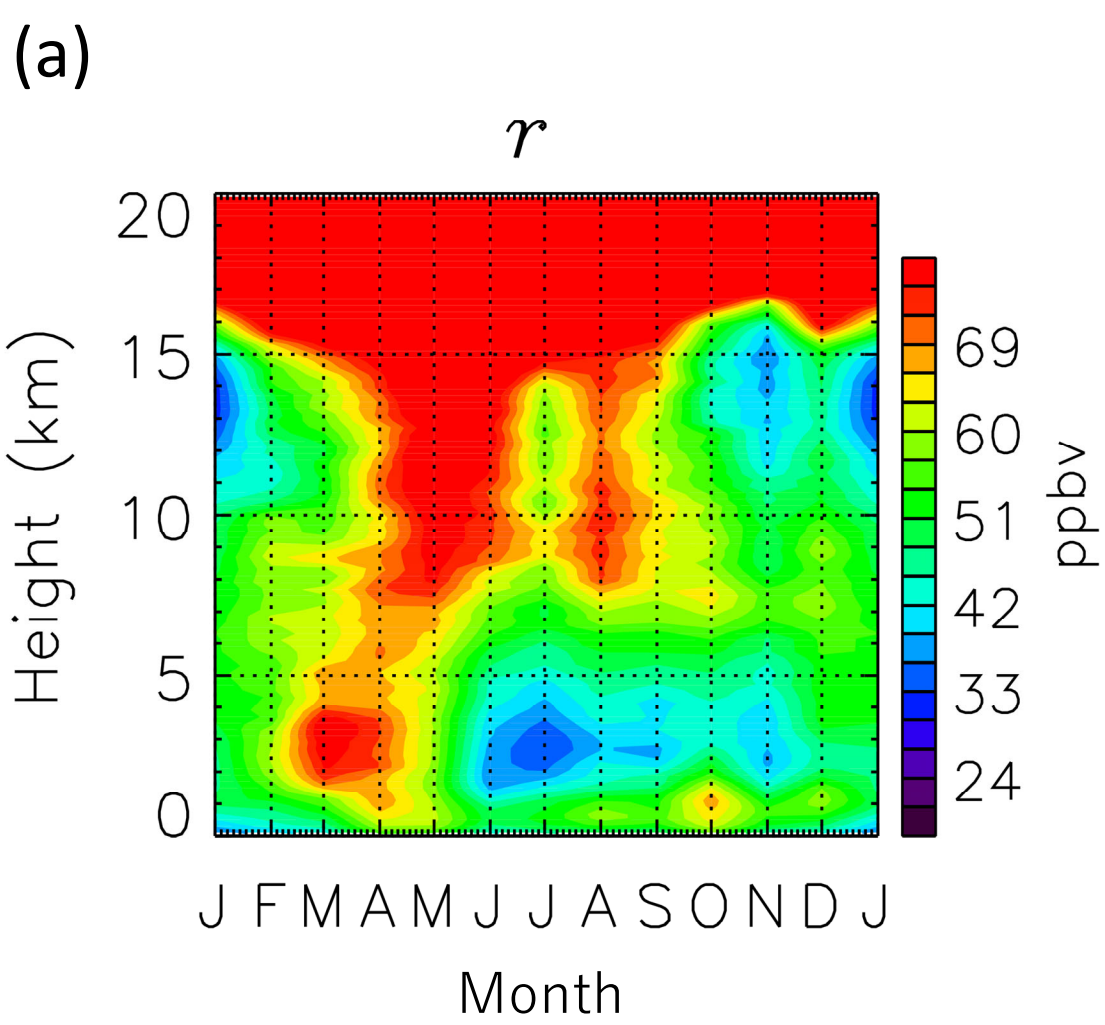
(a)
r
Height (km)
20
15
10
5
0
J F M A M J J A S O N D J
Month
69
60
51
42
33
24
ppbv

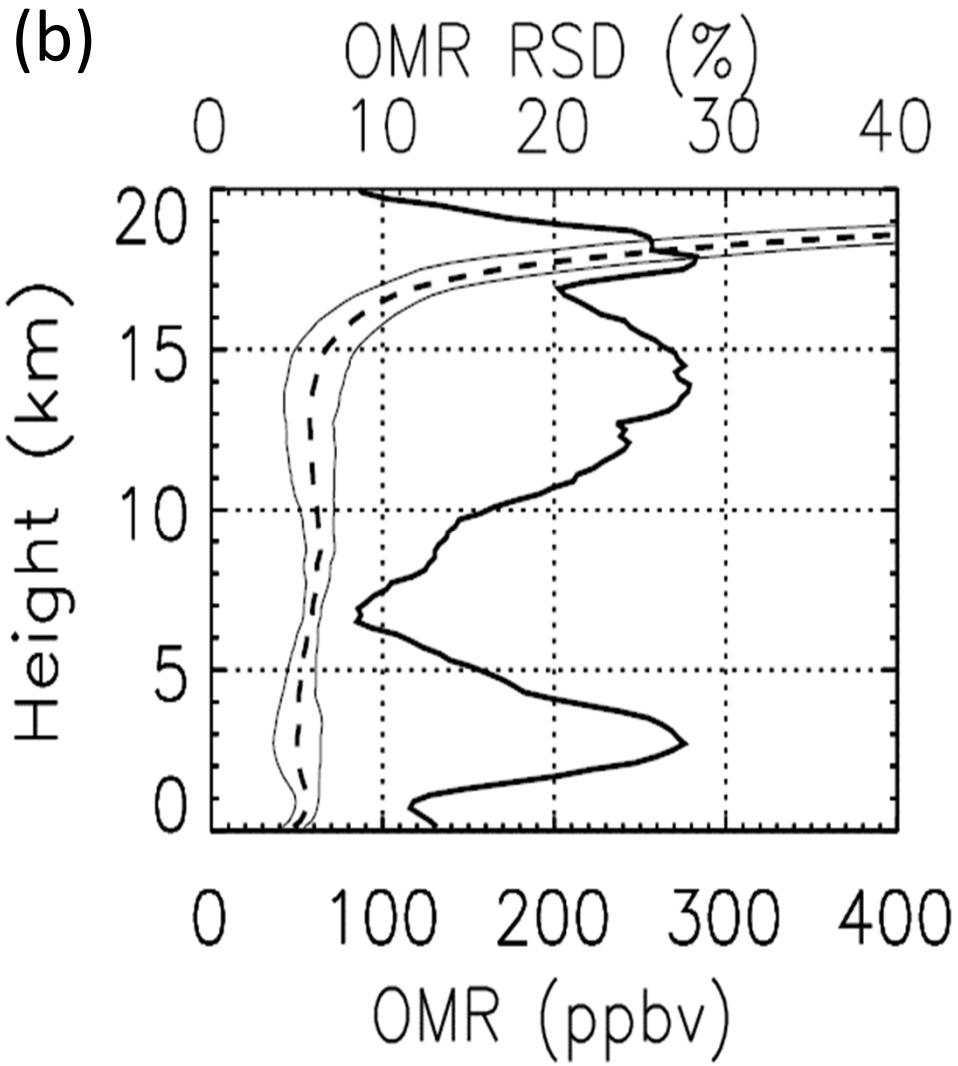
(b)
OMR RSD (%)
0
10
20
30
40
Height (km)
20
15
10
5
0
0
100
200
300
400
OMR (ppbv)

Figure 2.

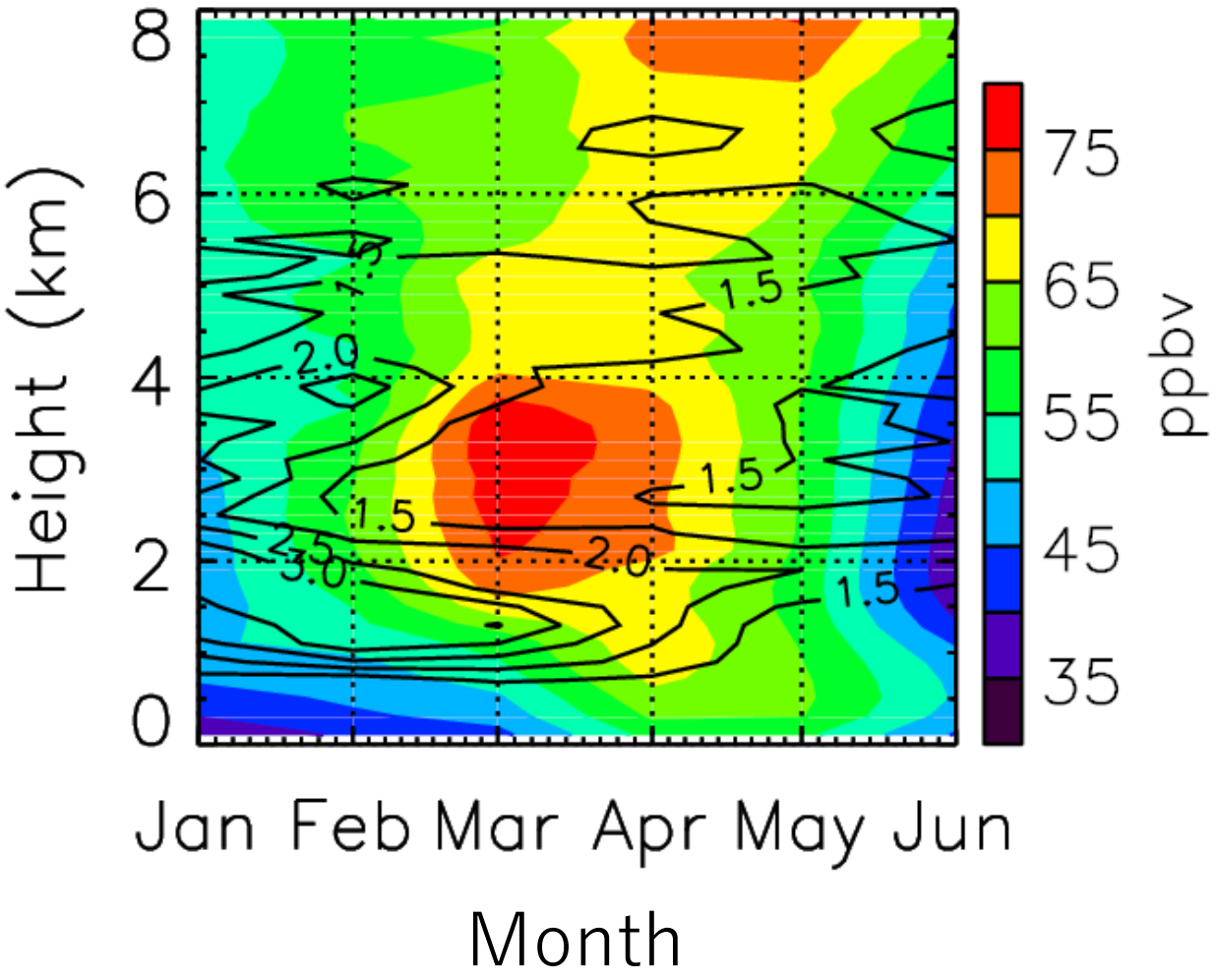
Height (km)
8
6
4
2
0
1.5
2.0
1.5
1.5
2.5
3.0
2.0
1.5
75
65
55
45
35
ppbv
Jan Feb Mar Apr May Jun
Month

Figure 3.

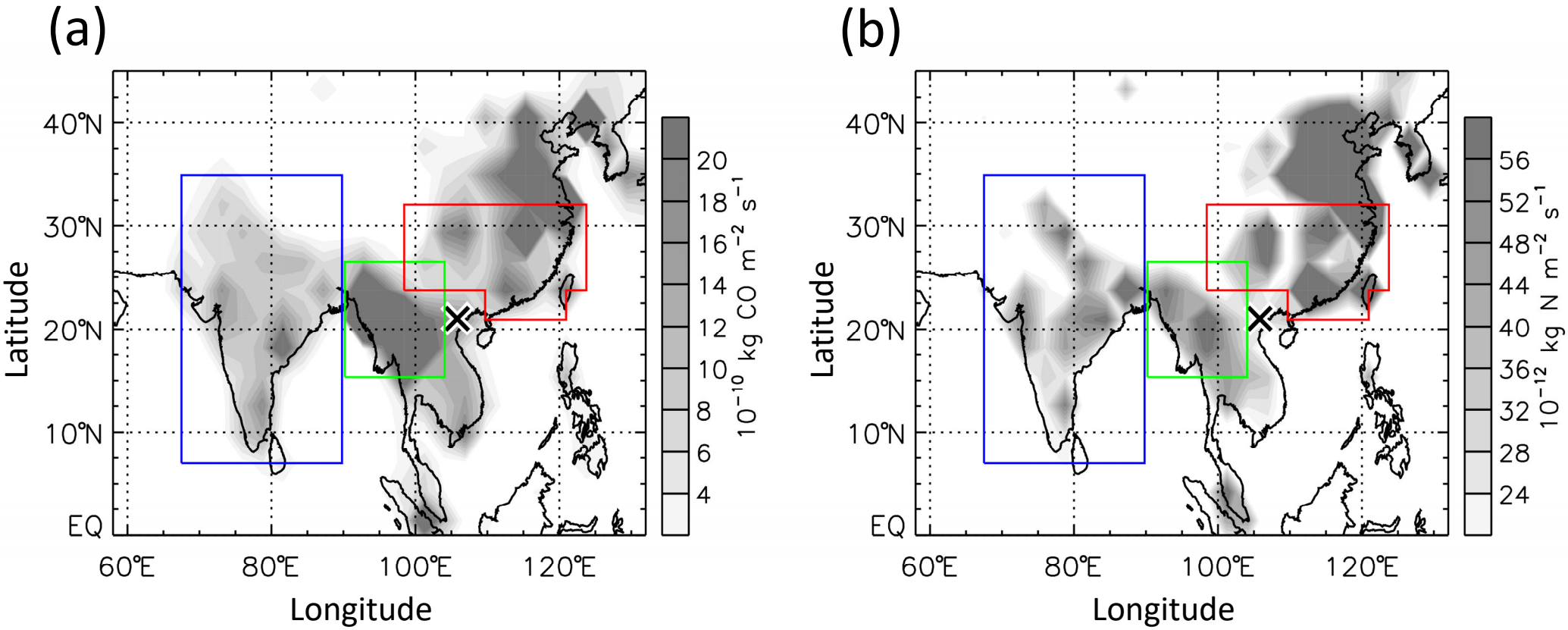
(a)
40°N
30°N
20°N
10°N
EQ
60°E
80°E
100°E
120°E
Latitude
Longitude
20
18
16
14
12
10
8
6
4
10^{-10} kg CO m^{-2} s^{-1}
(b)
40°N
30°N
20°N
10°N
EQ
60°E
80°E
100°E
120°E
Latitude
Longitude
56
52
48
44
40
36
32
28
24
10^{-12} kg N m^{-2} s^{-1}

Figure 4.

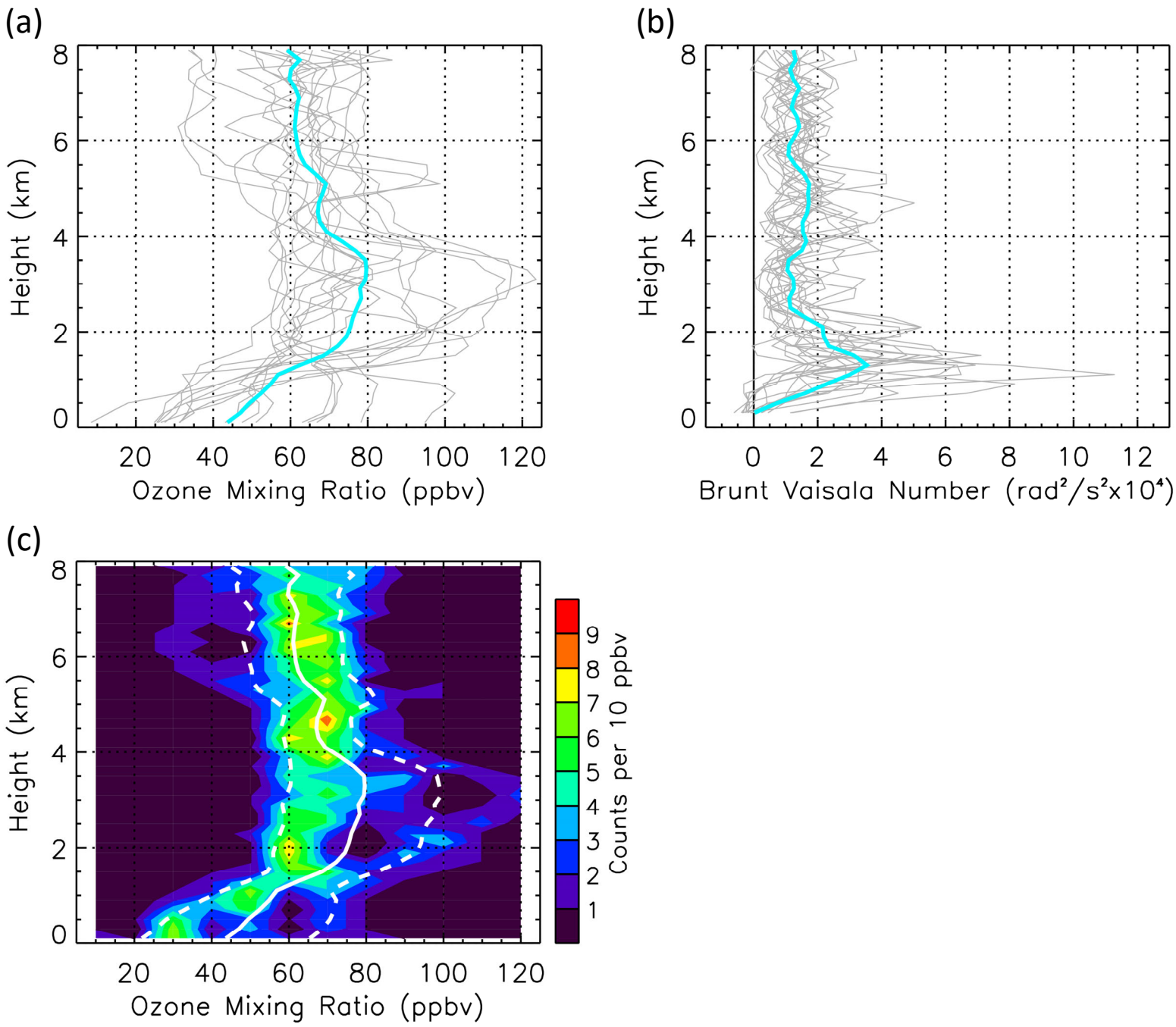
(a)
Height (km)
0
2
4
6
8
20
40
60
80
100
120
Ozone Mixing Ratio (ppbv)
(b)
Height (km)
0
2
4
6
8
0
2
4
6
8
10
12
Brunt Vaisala Number (rad²/s²x10⁴)
(c)
Height (km)
0
2
4
6
8
20
40
60
80
100
120
Ozone Mixing Ratio (ppbv)
Counts per 10 ppbv
1
2
3
4
5
6
7
8
9

Figure 5.

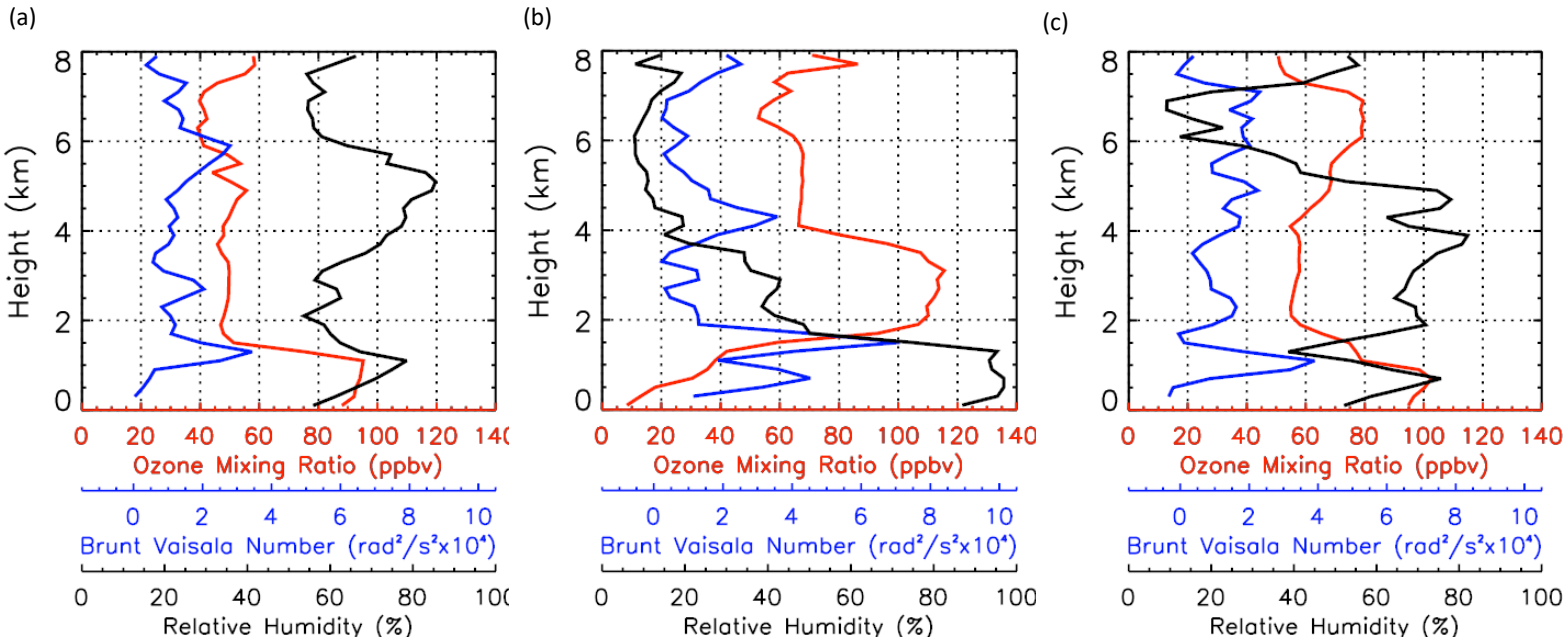
(a)
(b)
(c)
Height (km)
0
2
4
6
8
0 20 40 60 80 100 120 140
Ozone Mixing Ratio (ppbv)
0 2 4 6 8 10
Brunt Vaisala Number (rad²/s²x10⁴)
0 20 40 60 80 100
Relative Humidity (%)

Figure 6.

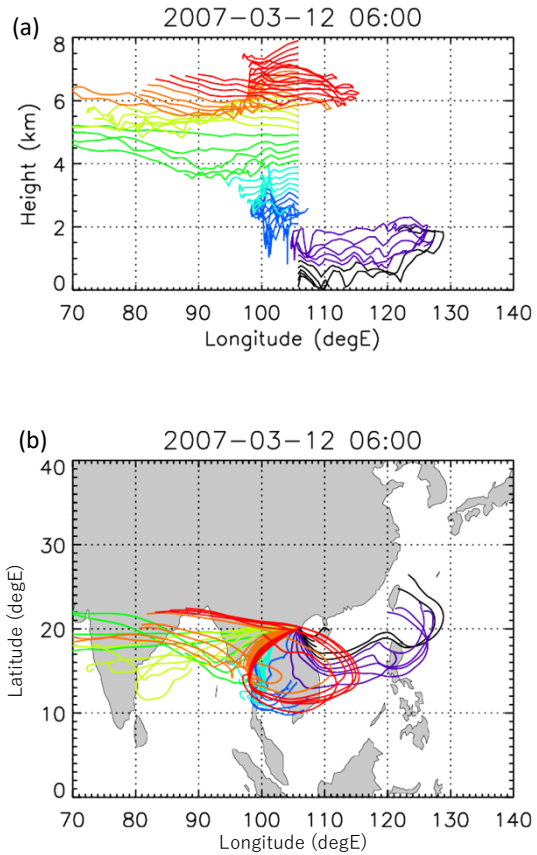
(a)
2007−03−12 06:00
Height (km)
0
2
4
6
8
70
80
90
100
110
120
130
140
Longitude (degE)
(b)
2007−03−12 06:00
Latitude (degE)
0
10
20
30
40
70
80
90
100
110
120
130
140
Longitude (degE)

Figure 7.

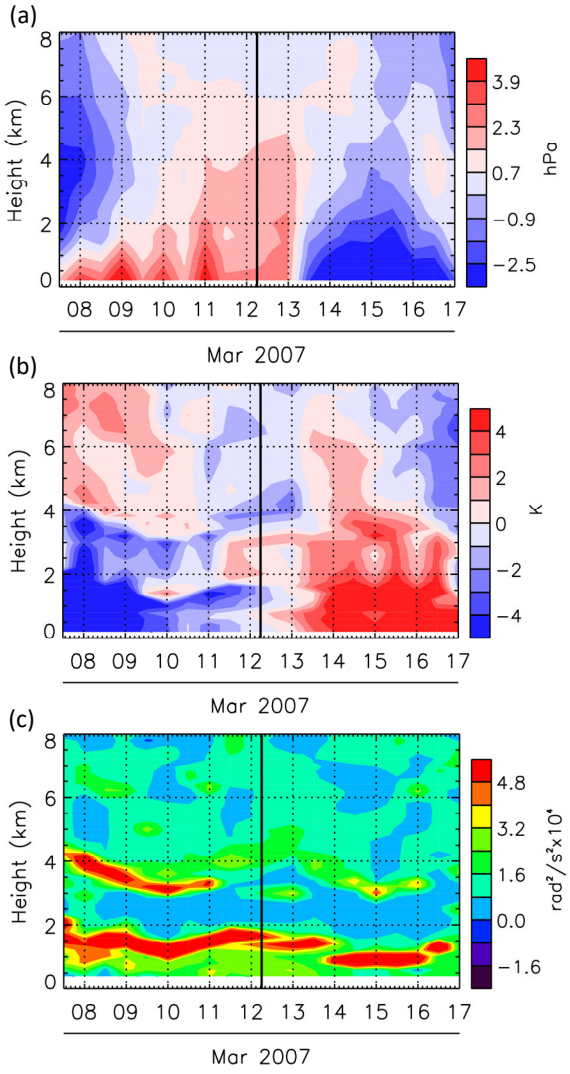
(a)
Height (km)
0
2
4
6
8
08 09 10 11 12 13 14 15 16 17
Mar 2007
3.9
2.3
0.7
−0.9
−2.5
hPa
(b)
Height (km)
0
2
4
6
8
08 09 10 11 12 13 14 15 16 17
Mar 2007
4
2
0
−2
−4
K
(c)
Height (km)
0
2
4
6
8
08 09 10 11 12 13 14 15 16 17
Mar 2007
4.8
3.2
1.6
0.0
−1.6
rad²/s²x10⁴

Figure 8.

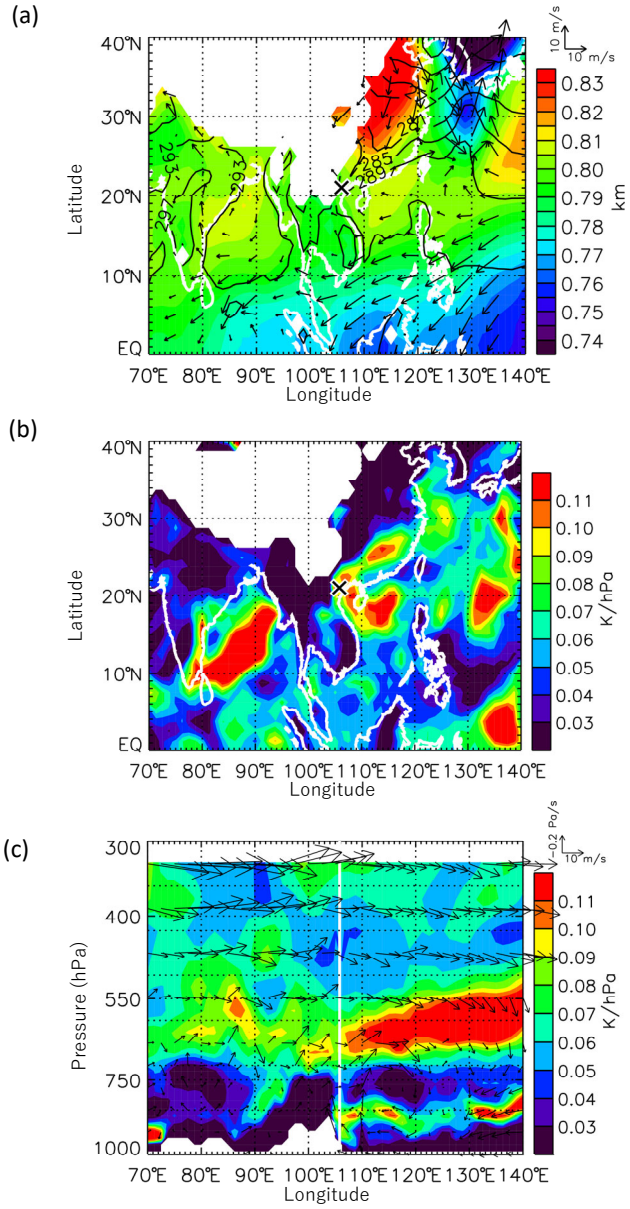
(a)
40°N
30°N
20°N
10°N
EQ
Latitude
70°E 80°E 90°E 100°E 110°E 120°E 130°E 140°E
Longitude
10 m/s
10 m/s
0.83
0.82
0.81
0.80
0.79
0.78
0.77
0.76
0.75
0.74
km
293
292
289
285
(b)
40°N
30°N
20°N
10°N
EQ
Latitude
70°E 80°E 90°E 100°E 110°E 120°E 130°E 140°E
Longitude
0.11
0.10
0.09
0.08
0.07
0.06
0.05
0.04
0.03
K/hPa
(c)
300
400
550
750
1000
Pressure (hPa)
70°E 80°E 90°E 100°E 110°E 120°E 130°E 140°E
Longitude
-0.2 Pa/s
10 m/s
0.11
0.10
0.09
0.08
0.07
0.06
0.05
0.04
0.03
K/hPa

Figure 9.

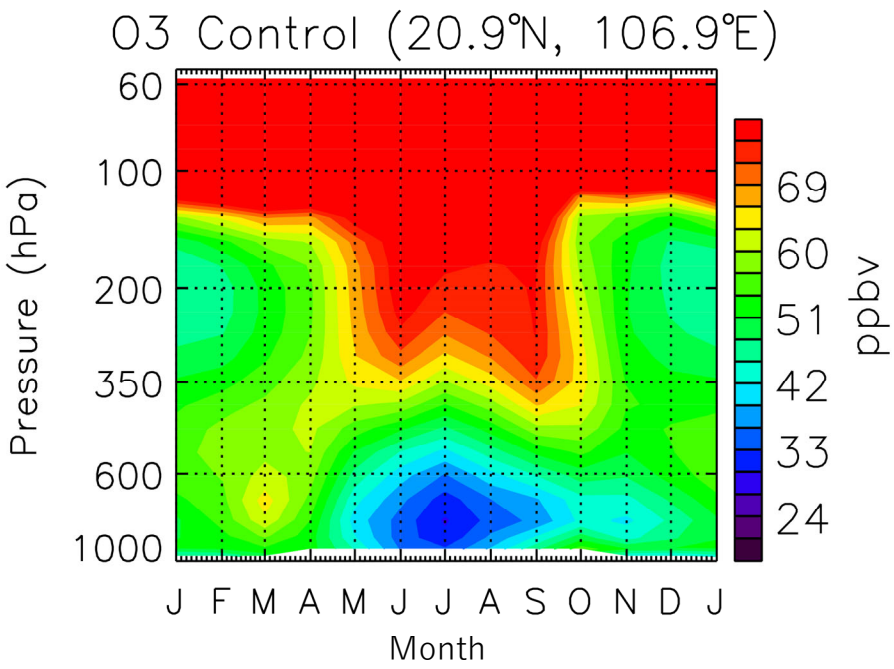
O3 Control (20.9°N, 106.9°E)
Pressure (hPa)
60
100
200
350
600
1000
J F M A M J J A S O N D J
Month
69
60
51
42
33
24
ppbv

Figure 10.

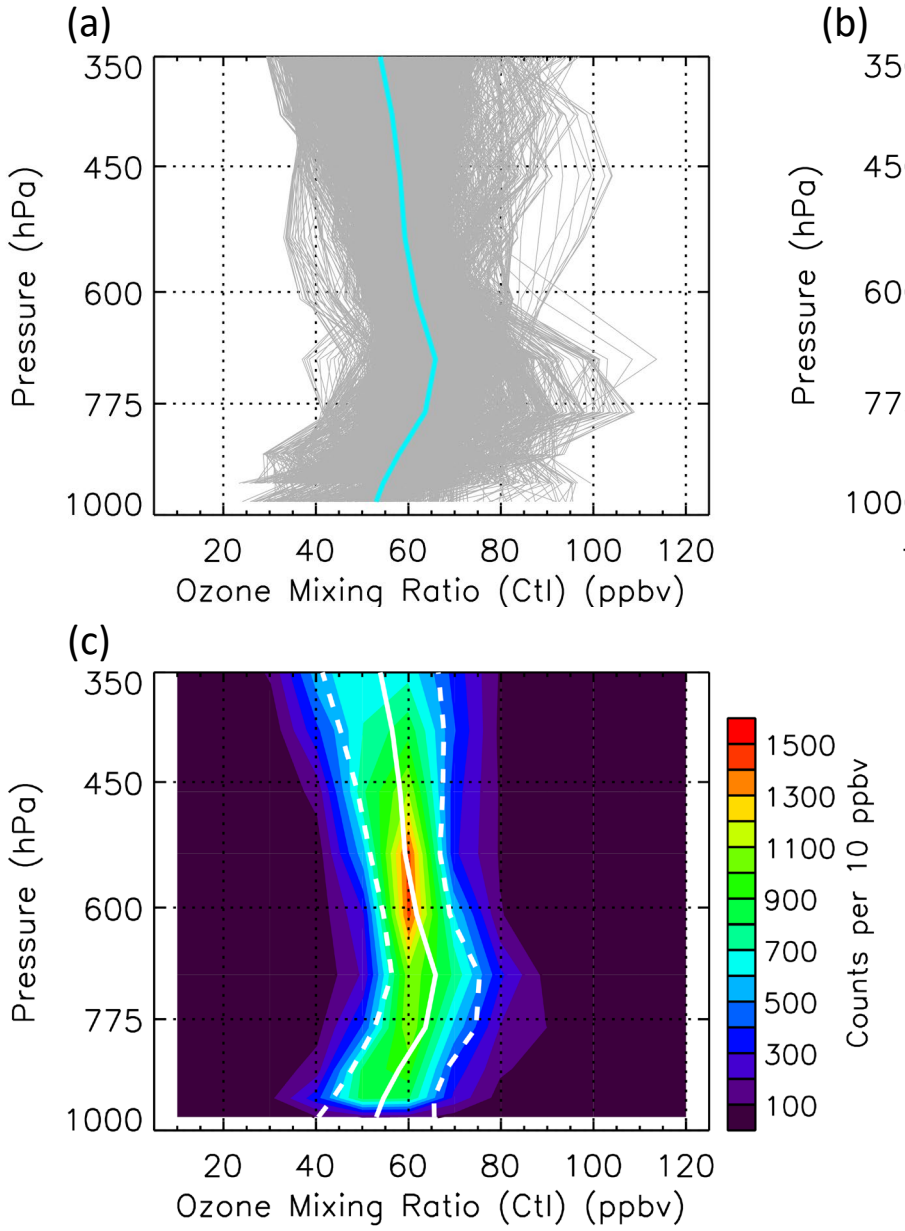
(a)
Pressure (hPa)
350
450
600
775
1000
20
40
60
80
100
120
Ozone Mixing Ratio (Ctl) (ppbv)
(b)
Pressure (hPa)
350
450
600
775
1000
−10
0
10
20
30
∂θ/∂p (10² K/hPa)
(c)
Pressure (hPa)
350
450
600
775
1000
20
40
60
80
100
120
Ozone Mixing Ratio (Ctl) (ppbv)
1500
1300
1100
900
700
500
300
100
Counts per 10 ppbv

Figure 11.

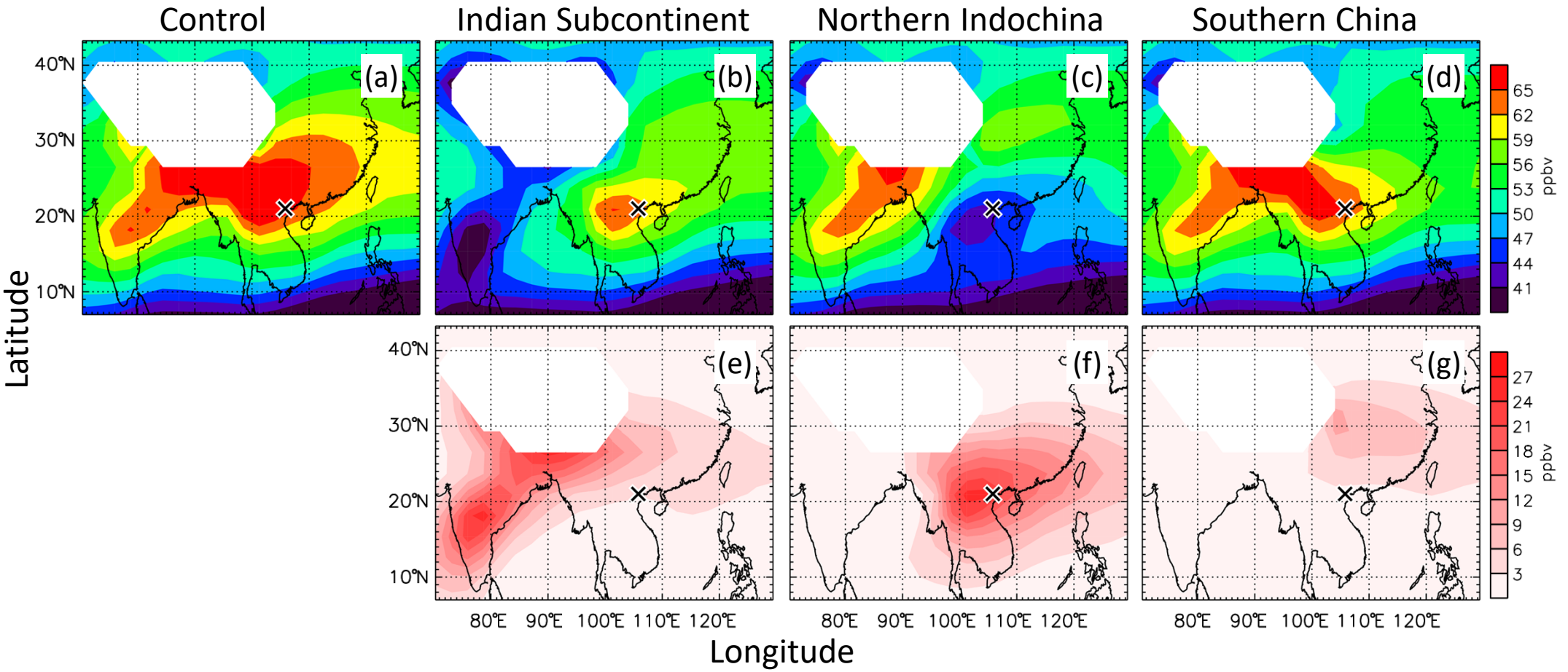
Control
Indian Subcontinent
Northern Indochina
Southern China
(a)
(b)
(c)
(d)
(e)
(f)
(g)
40°N
30°N
20°N
10°N
Latitude
80°E
90°E
100°E
110°E
120°E
Longitude
65
62
59
56
53
50
47
44
41
ppbv
27
24
21
18
15
12
9
6
3
ppbv

Figure 12.

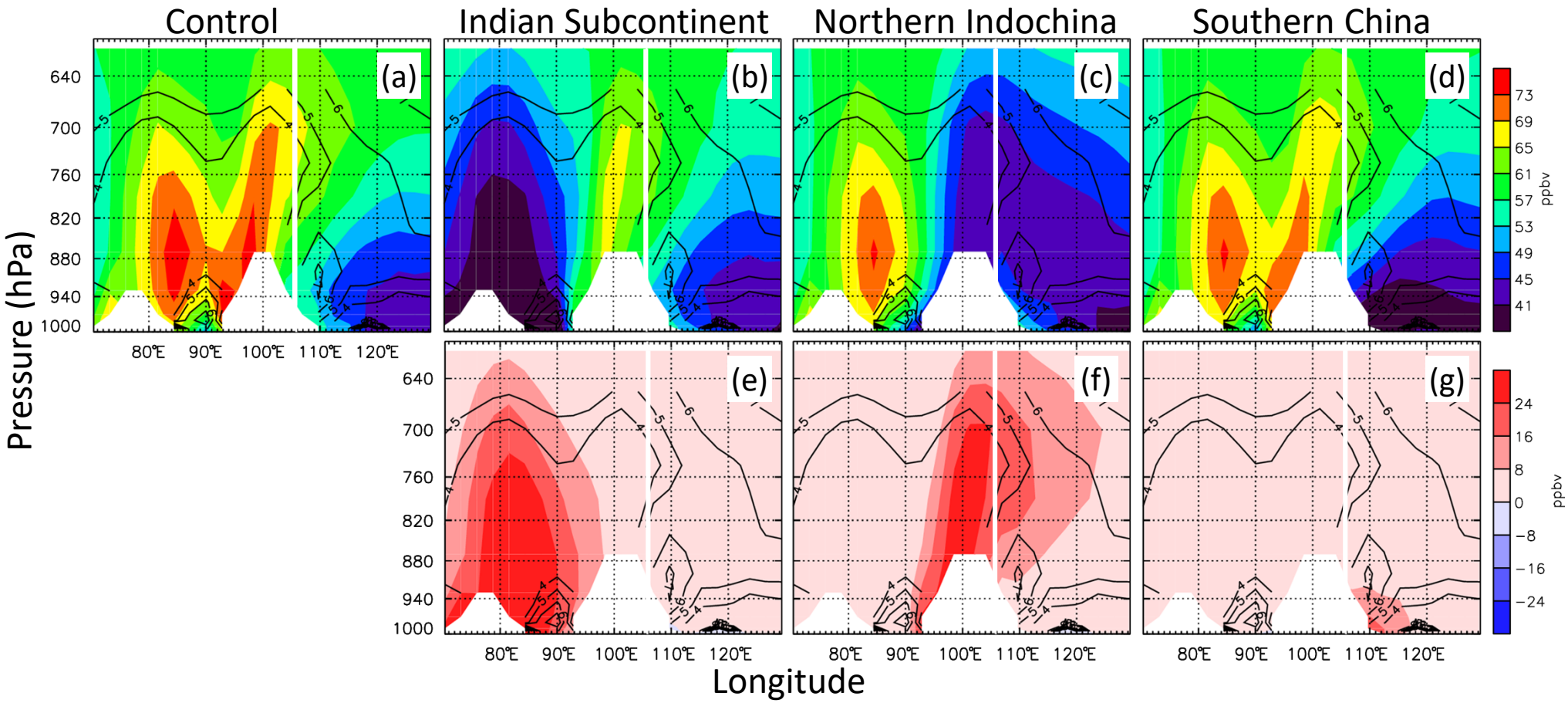
Control
Indian Subcontinent
Northern Indochina
Southern China
(a)
(b)
(c)
(d)
(e)
(f)
(g)
Pressure (hPa)
640
700
760
820
880
940
1000
80°E
90°E
100°E
110°E
120°E
Longitude
ppbv
73
69
65
61
57
53
49
45
41
24
16
8
0
−8
−16
−24

Figure 13.

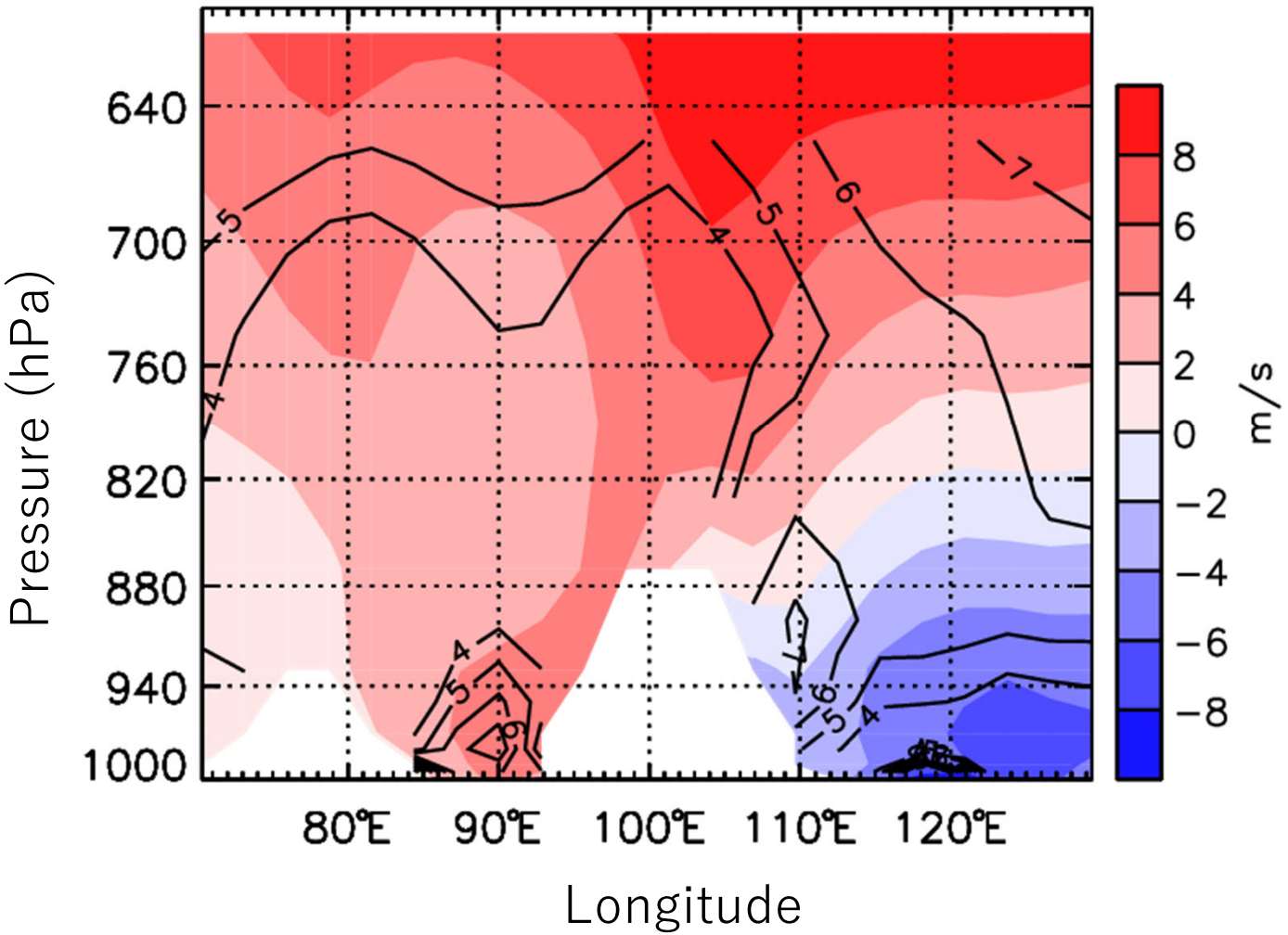
Pressure (hPa)
640
700
760
820
880
940
1000
80°E
90°E
100°E
110°E
120°E
Longitude
m/s
8
6
4
2
0
−2
−4
−6
−8

Figure 14.

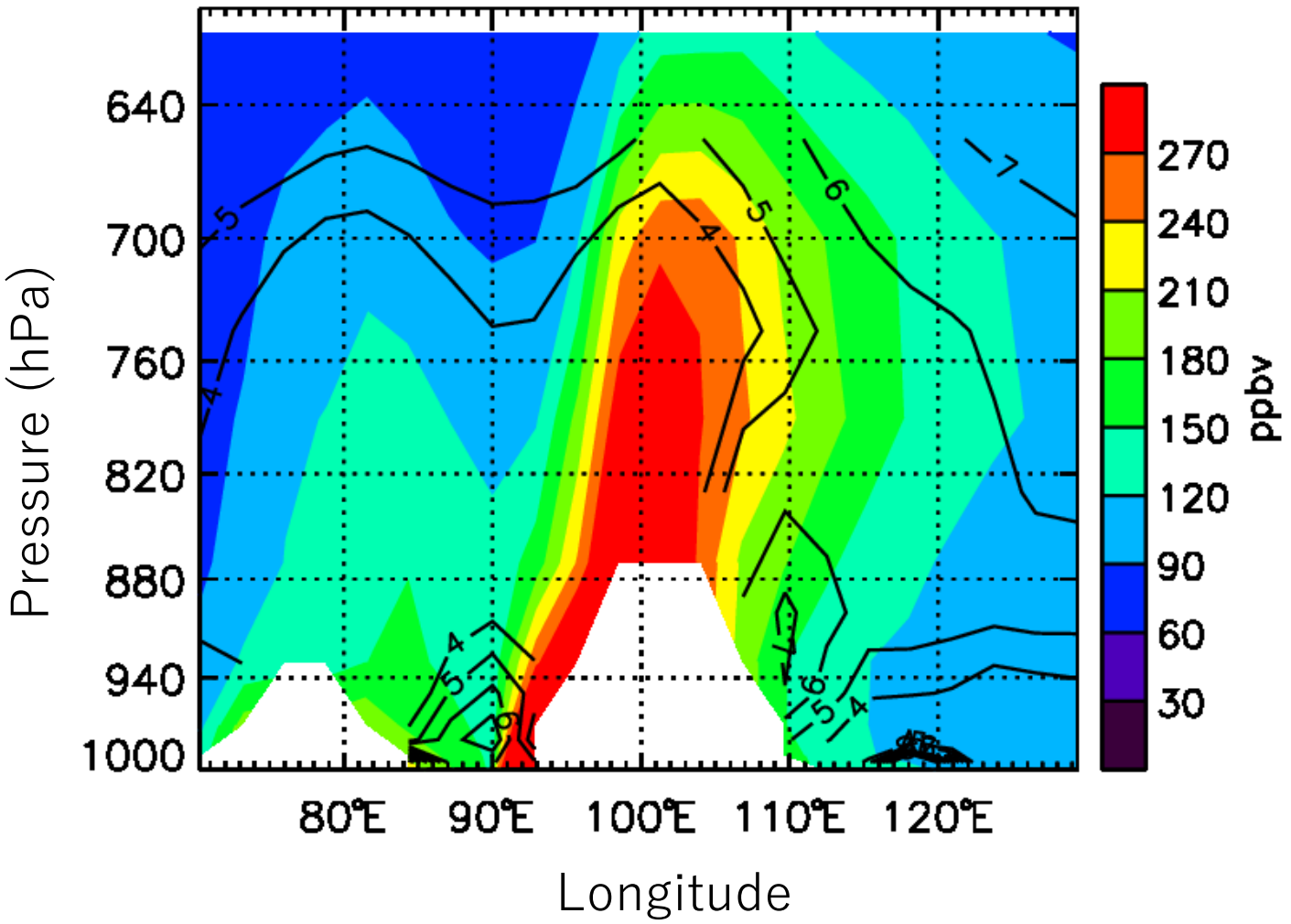
Pressure (hPa)
640
700
760
820
880
940
1000
80°E
90°E
100°E
110°E
120°E
Longitude
270
240
210
180
150
120
90
60
30
ppbv

Figure 15.

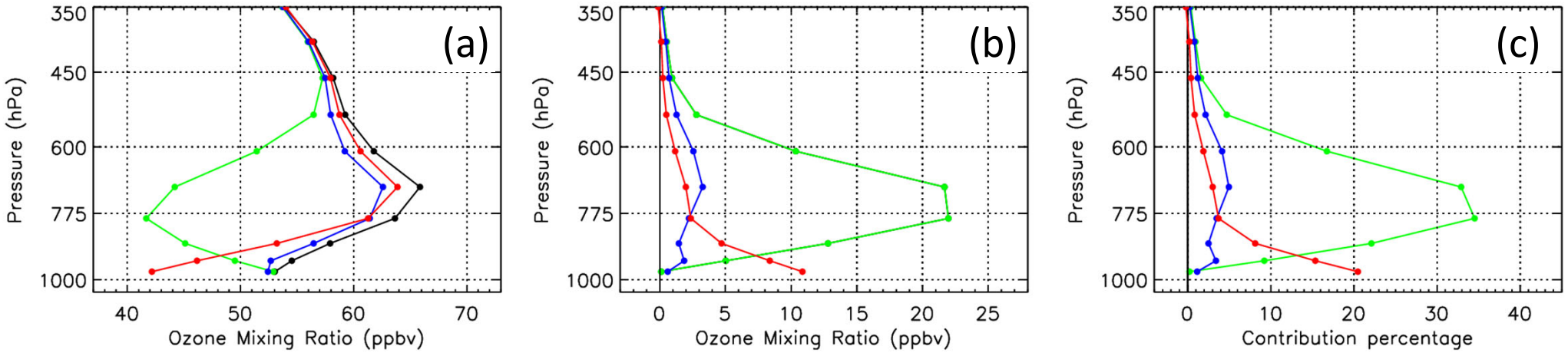
(a)
(b)
(c)
Pressure (hPa)
350
450
600
775
1000
40
50
60
70
Ozone Mixing Ratio (ppbv)
0
5
10
15
20
25
Ozone Mixing Ratio (ppbv)
0
10
20
30
40
Contribution percentage

Figure 16.

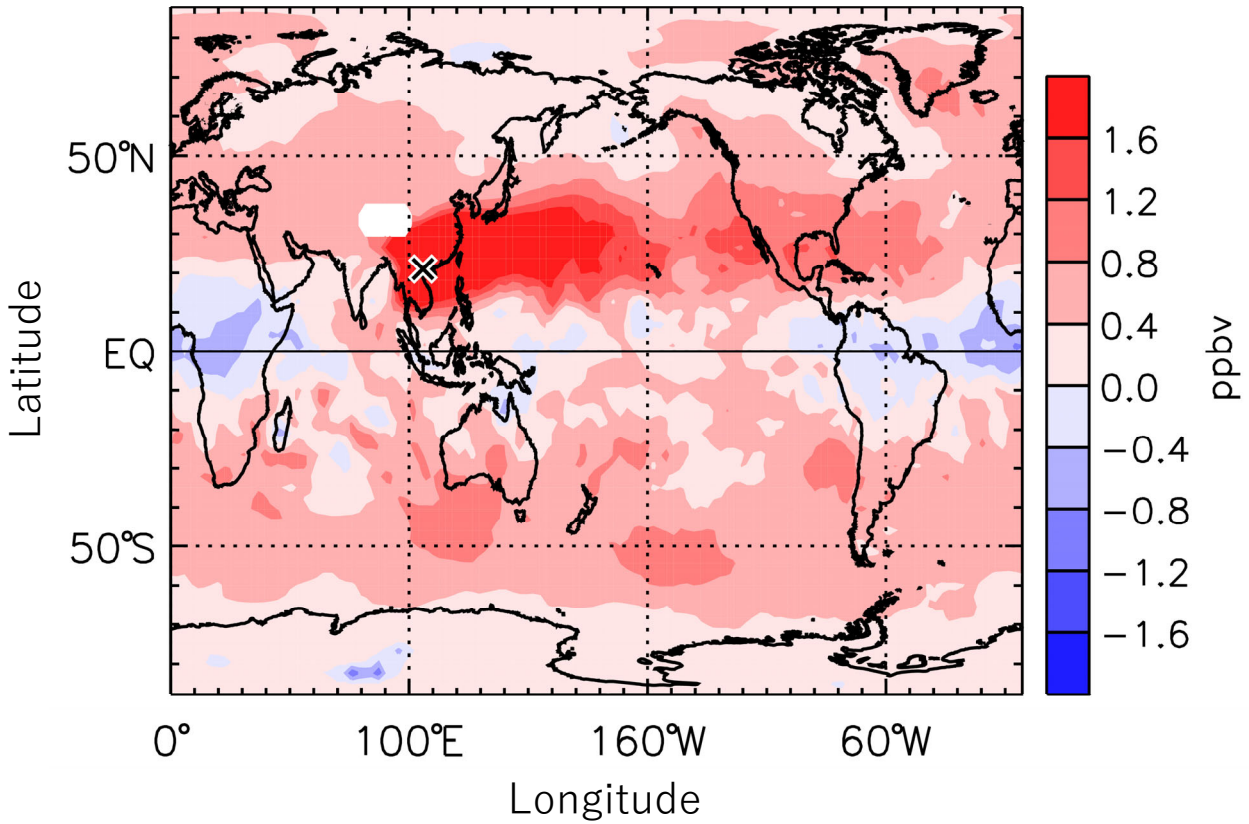
50°N
EQ
50°S
Latitude
0°
100°E
160°W
60°W
Longitude
1.6
1.2
0.8
0.4
0.0
−0.4
−0.8
−1.2
−1.6
ppbv

Figure 17.

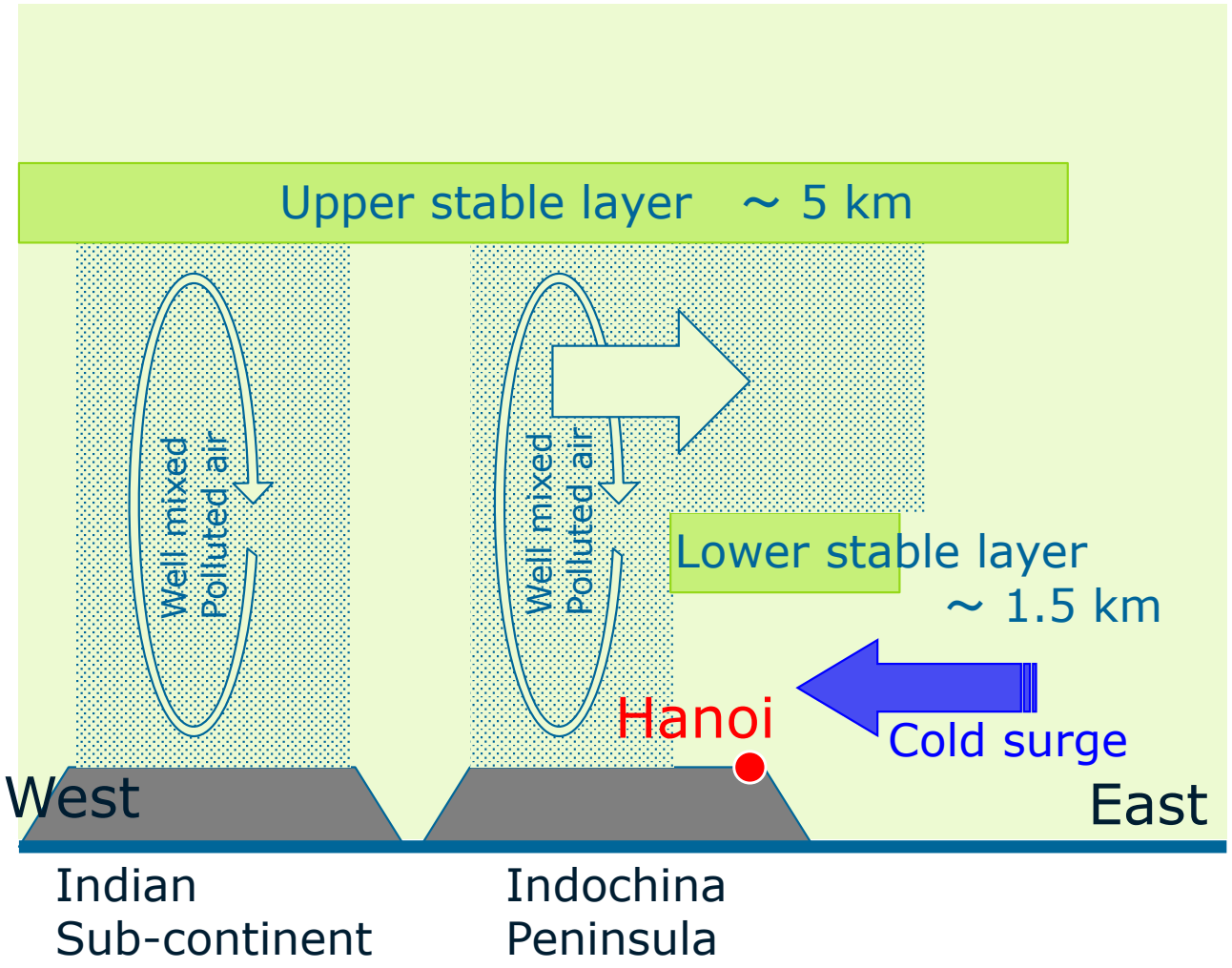
Upper stable layer ~ 5 km
Well mixed
Polluted air
Well mixed
Polluted air
Lower stable layer
~ 1.5 km
Hanoi
Cold surge
West
East
Indian
Sub-continent
Indochina
Peninsula